Tests of general relativity in the nonlinear regime: A parametrized plunge-merger-ringdown gravitational waveform model

Elisa Maggio,[1,*] Hector O. Silva,[1] Alessandra Buonanno,[1,2] and Abhirup Ghosh[1]
[1]*Max Planck Institute for Gravitational Physics (Albert Einstein Institute), D-14476 Potsdam, Germany*
[2]*Department of Physics, University of Maryland, College Park, Maryland 20742, USA*

(Received 24 January 2023; accepted 22 June 2023; published 20 July 2023)

The plunge-merger stage of the binary-black hole coalescence, when the bodies' velocities reach a large fraction of the speed of light and the gravitational-wave luminosity peaks, provides a unique opportunity to probe gravity in the dynamical and nonlinear regime. How much do the predictions of general relativity differ from the ones in other theories of gravity for this stage of the binary evolution? To address this question, we develop a parametrized waveform model, within the effective-one-body formalism, that allows for deviations from general relativity in the plunge-merger-ringdown stage. As first step, we focus on nonprecessing-spin, quasicircular black hole binaries. In comparison to previous works, for each gravitational wave mode, our model can modify, with respect to general-relativistic predictions, the instant at which the amplitude peaks, the instantaneous frequency at this time instant, and the value of the peak amplitude. We use this waveform model to explore several questions considering both synthetic-data injections and two gravitational wave signals. In particular, we find that deviations from the peak gravitational wave amplitude and instantaneous frequency can be constrained to about 20% with GW150914. Alarmingly, we find that GW200129_65458 shows a strong violation of general relativity. We interpret this result as a false violation, either due to waveform systematics (mismodeling of spin precession) or due to data-quality issues depending on one's interpretation of this event. This illustrates the use of parametrized waveform models as tools to investigate systematic errors in plain general relativity. The results with GW200129_65458 also vividly demonstrate the importance of waveform systematics and of glitch mitigation procedures when interpreting tests of general relativity with current gravitational wave observations.

DOI: 10.1103/PhysRevD.108.024043

I. INTRODUCTION

Remarkably, so far, the theory of general relativity (GR), introduced by Albert Einstein in 1915, has passed all available experimental and observational tests [1]: on cosmological [2] and short scales [3,4], in the low-velocity, weak-field [5] and strong-field settings [6–8], and in the dynamical, high-velocity and strong-field regime [9–13]. The latter has been probed, since 2015, through the gravitational wave (GW) observation of the coalescence of binary black holes (BBHs) [14–19], neutron-star–black-hole (BH) binaries [20], and binary neutron stars [21,22] by the LIGO and Virgo detectors [23,24].

Generally, tests of GR with GW observations have been developed following two strategies: theory independent and theory specific. The former assumes that the underlying GW signal is well-described by GR, and non-GR degrees of freedom (or parameters) are included to characterize any potential deviation. These tests use GW observations to check consistency with their nominal predictions in GR, and then constrain the non-GR parameters at a certain statistical level of confidence. Eventually, the non-GR parameters can be translated to the ones in specific modified theories of gravity, albeit there could be subtleties in doing it due to the choice of the priors and the actual parameters on which the measurements are done. By contrast, analyses that compare directly the data with proposed modified theories of gravity belong to the theory-specific framework of tests of GR.

Here, we focus on theory-independent tests of GR for BBHs. Historically, those tests have been proposed introducing deviations in (or parametrizations of) the gravitational waveform, whether for the inspiral, the merger or the ringdown stages, in time or frequency domain. Those parametrizations are clearly not unique;

*Corresponding author.
elisa.maggio@aei.mpg.de

neither they guarantee to fully represent the infinite space of modified gravity-theory waveforms. Furthermore, non-GR parameters may be degenerate with each other, limiting the study to a subset of them [9] or demanding the use of principal-component-analysis methods [25].

Many parametrized waveforms have been suggested in the literature, originally focusing on the inspiral phase [26–28], when the BBH system slowly but steadily looses energy through GW emission, and the bodies come closer and closer to each other until they merge. When the first frequency-domain models for the inspiral-merger-ringdown (IMR) waveforms in GR became available [29,30], a parametrized frequency-domain IMR waveform model was proposed in Ref. [31], variations of which were soon after employed in Ref. [32] for data-analysis explorations. Those initial works, together with other developments [33,34], are at the foundation of the Test Infrastructure for GEneral Relativity (TIGER) [35–37], Flexible Theory Independent (FTI) [38], `pSEOBNR` [39,40], and `pyRing` [41–43] pipelines, which today are routinely used by the LIGO-Virgo-KAGRA (LVK) Collaboration [9–13] to perform parametrized tests of GR, probing the generation of GWs and the remnant properties, in the linear and nonlinear strong-field gravity regime. Other theory-independent tests were also performed, e.g., in Refs. [44–51].

In this manuscript, we develop a parametrized time-domain IMR waveform model within the effective-one-body (EOB) formalism [52–59]. The EOB approach builds semianalytical IMR waveforms by combining analytical predictions for the inspiral [notably from post-Newtonian (PN), post-Minkowskian (PM), and gravitational self-force (GSF) approximations] and ringdown phases (from BH perturbation theory) with physically-motivated Ansätze for the plunge-merger stage. The EOB waveforms are then made highly accurate via a calibration to numerical relativity (NR) waveforms of BBHs. The EOB formalism relies on three key ingredients: the EOB conservative dynamics (i.e., a two-body Hamiltonian), the EOB radiation-reaction forces (i.e., the energy and angular momentum fluxes) and the EOB GW modes. Since the EOB waveforms are computed on the EOB dynamics by solving Hamilton's equations, in principle deviations from GR can be introduced in all the three building blocks, consistently. Here, for simplicity, following previous work [39,40] which focused on the ringdown stage, we introduce non-GR parameters in the plunge-merger-ringdown GW modes. We leave to future work the extension of the parametrization to the conservative and dissipative dynamics, notably by including in the EOB dynamics fractional deviations to the PN (as well as PM and GSF) terms, to NR-informed terms or specific new terms motivated by phenomena observed in modified gravity theories. We note that non-GR deviations in the EOB energy flux were implemented in Refs. [60,61], and the corresponding EOB waveforms were used in IMR consistency and other tests of gravity in Refs. [60–62].

Although the parametrized IMR model can in principle be constructed for precessing spinning BBHs, as first step, we consider nonprecessing BHs. There are two main EOB families, `SEOBNR` (e.g., see Refs. [63–65]) and `TEOBResumS` (e.g., see Refs. [66–68]). We consider here the former, and in particular we focus on the `SEOBNRHM` model developed in Refs. [63,64], which contains GW modes beyond the dominant quadrupole. We denote the parametrized version `pSEOBNRHM`. In Fig 1, we contrast a GR `SEOBNRHM` waveform with parameters similar to the first GW observation, GW150914, with a `pSEOBNRHM` waveform where the fractional deviations from GR are of the order of a few tens of percent. We can see that differences from GR occur just before, during, and after the merger stage, which is when the gravitational strain peaks.

The paper is organized as follows. In Sec. II, we describe how we build the `pSEOBNRHM` model starting from the baseline model `SEOBNRHM`, and introduce the non-GR parameters that describe potential deviations from GR during the plunge-merger-ringdown stage. In Sec. III, we study in detail the morphology of the parametrized

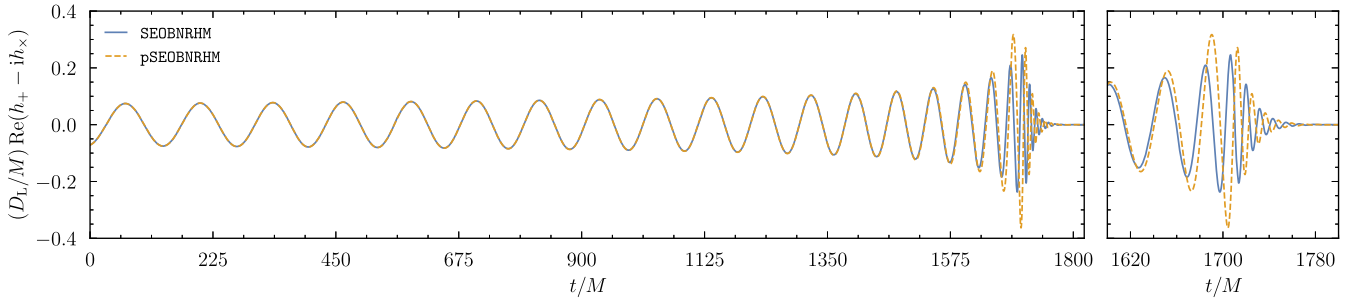

FIG. 1. Illustrative BBH waveform obtained with the `pSEOBNRHM` model introduced here (dashed line) and the corresponding baseline model `SEOBNRHM` [64,71,86] (solid line) for a face-on, nonspinning and quasicircular binary with GW150914-like mass-ratio $q = m_2/m_1 \approx 0.867$, and detector-frame total mass $M = m_1 + m_2 = 71.9M_\odot$. The `pSEOBNRHM` waveform is generated with non-GR parameters values $\delta\Delta t = -0.2$, $\delta\omega = -0.4$, and $\delta A = 0.5$. These parameters change respectively, in comparison to GR, the instant at which the GW amplitude peaks, the orbital frequency at this time instant, and the value of the peak amplitude. Both waveforms are phase aligned and time shifted around 20 Hz using the prescription of Refs. [59,86,89,90]. The details of how the waveform model is developed are in given Sec. II, and additional details about its morphology are presented in Sec. III.

waveform, and understand which parts of the waveform change when the non-GR parameters are varied one at the time. After discussing the basics of Bayesian analysis in Sec. IV, we perform a synthetic-signal injection study in Sec. V, and then apply our parametrized IMR model to real data in Secs. VI and VII, analyzing two events, GW150914 and GW200129. Finally, we summarize our conclusions and future work in Sec. VIII.

Unless stated otherwise, we work in geometrical units in which $G = 1 = c$.

II. THE PARAMETRIZED PLUNGE-MERGER-RINGDOWN WAVEFORM MODEL

In this section we first review the GR waveform model developed within the EOB formalism. In Sec. II B, we explain how we deform this baseline model by introducing deformations away from GR in the plunge-merger-ringdown phase.

A. A brief review of the effective-one-body gravitational waveform model

The GW signal produced by a spinning, nonprecessing, and quasicircular BBH with component masses m_1 and m_2, and total mass $M = m_1 + m_2$, is described in GR by a set of eleven parameters, $\vartheta_{\rm GR}$, given by

$$\vartheta_{\rm GR} = \{m_1, m_2, \chi_1, \chi_2, \iota, \psi, \alpha, \delta, D_{\rm L}, t_c, \phi_c\}, \tag{2.1}$$

where χ_i ($i = 1, 2$) are the constant-in-time projections of each BH's spin vectors $\boldsymbol{S}_i$ in the direction of the unit vector perpendicular to the orbital plane $\hat{\boldsymbol{L}}$, i.e., $\chi_i = \boldsymbol{S}_i \cdot \hat{\boldsymbol{L}}/m_i^2$, where $|\chi_i| \leq 1$, (ι, ψ) describe the binary's orientation through the inclination and polarization angles, (α, δ) describe the sky location of the source in the detector frame, $D_{\rm L}$ is the luminosity distance, and t_c and ϕ_c are the reference time and phase, respectively. It is convenient to define the chirp mass $\mathcal{M} = M\nu^{3/5}$, where $\nu = m_1 m_2/M^2$ is the symmetric mass ratio, the asymmetric mass ratio $q = m_2/m_1$, and the effective spin $\chi_{\rm eff} = (\chi_1 m_1 + \chi_2 m_2)/M$. We adopt the convention that $m_1 \geq m_2$ and thus $q \leq 1$.

The GW polarizations can be written in the observer's frame as

$$h_+(\iota, \varphi_0; t) - \mathrm{i} h_\times(\iota, \varphi_0; t) = \sum_{\ell=2}^{\infty} \sum_{m=-\ell}^{\ell} {}_{-2}Y_{\ell m}(\iota, \varphi_0) h_{\ell m}(t), \tag{2.2}$$

where φ_0 is the azimuthal direction of the observer, where, without loss of generality, we set $\varphi_0 = \phi_c$, and ${}_{-2}Y_{\ell m}$ are the -2 spin-weighted spherical harmonics [69], ℓ is the angular number and $|m| \leq \ell$ is the azimuthal number of each GW mode, $h_{\ell m}$.

We follow Refs. [40,70] and use as our baseline model (i.e., the waveform model upon which the non-GR deviation parameters are added) the time-domain IMR waveform developed in Refs. [63,64,71] within the EOB formalism [52–59], `SEOBNRv4HM_PA`.[1] The model uses the postadiabatic (PA) approximation, which was originally introduced in Refs. [74–76] (and also subsequently used in the `TEOBResumS` waveform models) to speed up the generation of the time-domain waveforms for spinning, nonprecessing, and quasicircular compact binaries. It includes the $(\ell, |m|) = (2,2)$, (2, 1), (3, 3), (4, 4), and (5, 5) GW modes. For nonprecessing BBHs (i.e., with component spins aligned or antialigned with the orbital angular momentum), we have that $h_{\ell m} = (-1)^\ell h^*_{\ell -m}$. Hence, we can consider $m > 0$ without loss of generality. Hereafter, we refer to `SEOBNRv4HM_PA` as `SEOBNRHM` for brevity.

As explained in Refs. [63,64], the `SEOBNRHM` waveform is constructed by attaching the merger-ringdown waveform, $h^{\rm merger-RD}_{\ell m}(t)$, to the inspiral-plunge waveform, $h^{\rm insp-plunge}_{\ell m}(t)$, at a matching time $t = t^{\ell m}_{\rm match}$,

$$h_{\ell m}(t) = h^{\rm insp-plunge}_{\ell m}(t)\Theta(t^{\ell m}_{\rm match} - t) + h^{\rm merger-RD}_{\ell m}(t)\Theta(t - t^{\ell m}_{\rm match}), \tag{2.3}$$

where $\Theta(t)$ is the Heaviside step function and the value of $t^{\ell m}_{\rm match}$ is defined as

$$t^{\ell m}_{\rm match} = \begin{cases} t^{22}_{\rm peak}, & (\ell, m) = (2,2), (3,3), (2,1), (4,4) \\ t^{22}_{\rm peak} - 10M, & (\ell, m) = (5,5), \end{cases} \tag{2.4}$$

where $t^{22}_{\rm peak}$ is the time at which the amplitude of the (2, 2) mode [i.e., $h_{22}(t)$ in Eq. (2.2)] has its maximum value. We impose that the amplitude and phase of $h_{\ell m}(t)$ at $t = t^{\ell m}_{\rm match}$ are C^1 (i.e., they are continuously and differentiable at this time instant). The time $t^{22}_{\rm peak}$ is defined as

$$t^{22}_{\rm peak} = t^{\Omega}_{\rm peak} + \Delta t^{22}_{\rm peak}, \tag{2.5}$$

where $t^{\Omega}_{\rm peak}$ is the time in which the EOB orbital frequency peaks [77]. Calculations performed in the test-particle limit using BH perturbation theory found that the amplitude and the orbital frequency peak at different times, especially when the central BH has large spins [78–81]. This

[1]The model's name indicates that the EOB model (`EOB`) is calibrated to NR simulations (`NR`), includes spin effects (`S`), contains high-order radiation modes (`HM`), and uses the post-adiabatic approximation (`PA`) to reduce the waveform generation time. The version of the model used here is `v4`. The first version of this waveform family is the nonspinning `EOBNRv1` model of Refs. [72,73].

motivates the introduction of the time-lag parameter $\Delta t^{22}_{\rm peak}$ in Eq. (2.5), which can be fitted against NR waveforms as function of the symmetric mass ratio ν and the BH's spins $\chi_{1,2}$ (see Sec. II B in Ref. [63] for details). We impose the condition $\Delta t^{22}_{\rm peak} \leq 0$ to ensure that the attachment of the merger-ringdown waveform happens before the peak of the orbital frequency, and thus before the end of the binary's dynamics. For later convenience, we define

$$\Delta t^{\rm GR}_{\ell m} = -\Delta t^{22}_{\rm peak}. \tag{2.6}$$

Because we are interested in adding non-GR terms to $h^{\rm merger-RD}_{\ell m}(t)$, we now briefly review how the merger-ringdown waveform is constructed. Further details can be found in Sec. IV E of Ref. [64]. The merger-ringdown mode is written as

$$h^{\rm merger-RD}_{\ell m} = \nu \tilde{A}_{\ell m}(t) e^{{\rm i}\tilde{\phi}_{\ell m}(t)} e^{{\rm i}\sigma_{\ell m0}(t-t^{\ell m}_{\rm match})}, \tag{2.7}$$

where $\sigma_{\ell m0}$ are the complex-valued frequencies of the least damped quasinormal mode (QNM) of the remnant BH [82–84]. We define $\sigma^{\rm R}_{\ell m0} = {\rm Im}(\sigma_{\ell m0}) < 0$ and $\sigma^{\rm I}_{\ell m0} = -{\rm Re}(\sigma_{\ell m0}) < 0$. The functions $\tilde{A}_{\ell m}$ and $\tilde{\phi}_{\ell m}$ are given by [63]

$$\tilde{A}_{\ell m} = c^{\ell m}_{1,c} \tanh[c^{\ell m}_{1,f}(t - t^{\ell m}_{\rm match}) + c^{\ell m}_{2,f}] + c^{\ell m}_{2,c}, \tag{2.8a}$$

$$\tilde{\phi}_{\ell m} = \phi^{\ell m}_{\rm match} - d^{\ell m}_{1,c} \log\left[\frac{1 + d^{\ell m}_{2,f} e^{-d^{\ell m}_{1,f}(t-t^{\ell m}_{\rm match})}}{1 + d^{\ell m}_{2,f}}\right], \tag{2.8b}$$

where $\phi^{\ell m}_{\rm match}$ is the phase of the inspiral-plunge mode $h^{\rm insp-plunge}_{\ell m}$ at $t = t^{\ell m}_{\rm match}$. We see that Eq. (2.8) depend on the set of parameters $c^{\ell m}_i$ and $d^{\ell m}_i$ $(i = 1, 2)$, which are either constrained by imposing that $\tilde{A}_{\ell m}$, $\tilde{\phi}_{\ell m}$ are C^1 at $t = t^{\ell m}_{\rm match}$ (we append the subscript "c") or free parameters to be determined by fitting against NR waveforms (we append the subscript "f").

We now impose that $h_{\ell m}$ is C^1 at $t = t^{\ell m}_{\rm match}$. This yields two equations that relate the constrained coefficients $c^{\ell m}_{1,c}$ and $c^{\ell m}_{2,c}$ to the free coefficients $c^{\ell m}_{1,f}$, $c^{\ell m}_{2,f}$, to $\sigma^{\rm R}_{\ell m0}$ and to the mode amplitude of $h^{\rm insp-plunge}_{\ell m}$ and its first time derivative at the matching time, namely $|h^{\rm insp-plunge}_{\ell m}(t^{\ell m}_{\rm match})|$ and $\partial_t |h^{\rm insp-plunge}_{\ell m}(t^{\ell m}_{\rm match})|$. The equations are

$$\begin{aligned} c^{\ell m}_{1,c} = \frac{1}{\nu c^{\ell m}_{1,f}} &[\partial_t |h^{\rm insp-plunge}_{\ell m}(t^{\ell m}_{\rm match})| \\ &- \sigma^{\rm R}_{\ell m0} |h^{\rm insp-plunge}_{\ell m}(t^{\ell m}_{\rm match})|] \cosh^2 c^{\ell m}_{2,f}, \end{aligned} \tag{2.9a}$$

$$\begin{aligned} c^{\ell m}_{2,c} = &-\frac{1}{\nu} |h^{\rm insp-plunge}_{\ell m}(t^{\ell m}_{\rm match})| \\ &+ \frac{1}{\nu c^{\ell m}_{1,f}} [\partial_t |h^{\rm insp-plunge}_{\ell m}(t^{\ell m}_{\rm match})| \\ &- \sigma^{\rm R}_{\ell m0} |h^{\rm insp-plunge}_{\ell m}(t^{\ell m}_{\rm match})|] \cosh c^{\ell m}_{2,f} \sinh c^{\ell m}_{2,f}. \end{aligned} \tag{2.9b}$$

We also obtain one equation that relates the constrained parameter $d^{\ell m}_{1,c}$ to the free coefficients $d^{\ell m}_{1,f}$, $d^{\ell m}_{2,f}$, to $\sigma^{\rm I}_{\ell m0}$ and to the angular frequency of $h^{\rm insp-plunge}_{\ell m}$ at the matching time. The latter is defined as $\omega_{\ell m} = {\rm d}\phi^{\rm insp-plunge}_{\ell m}/{\rm d}t$, where $\phi^{\rm insp-plunge}_{\ell m} = \arg(h^{\rm insp-plunge}_{\ell m})$ is the phase of the inspiral-plunge GW mode. The equation is

$$d^{\ell m}_{1,c} = [\omega^{\rm insp-plunge}_{\ell m}(t^{\ell m}_{\rm match}) - \sigma^{\rm I}_{\ell m0}] \frac{1 + d^{\ell m}_{2,f}}{d^{\ell m}_{1,f} d^{\ell m}_{2,f}}. \tag{2.10}$$

The values of

$$|h^{\rm insp-plunge}_{\ell m}|, \qquad \partial_t |h^{\rm insp-plunge}_{\ell m}|, \quad \text{and} \quad \omega^{\rm insp-plunge}_{\ell m},$$

at $t = t^{\ell m}_{\rm match}$ are fixed by the so-called nonquasicircular (NQC) terms, $N_{\ell m}(t)$. The NQC terms describe nonquasicircular corrections to the modes during the late inspiral and plunge. The NQCs are a parametrized time series that is multiplied with the factorized PN GR modes, $h^{\rm F}_{\ell m}$, such that the resultant time series is calibrated against NR simulations. They are crucial in guaranteeing a very good agreement of the SEOBNRHM amplitude and phase (relative to NR) during the late inspiral and plunge.

The GW modes in the inspiral-plunge part of the EOB waveform are given as

$$h^{\rm insp-plunge}_{\ell m}(t) = h^{\rm F}_{\ell m}(t) N_{\ell m}(t), \tag{2.11}$$

where we refer the reader to Sec. IV C in Ref. [64] for details on how $h^{\rm F}_{\ell m}$ and $N_{\ell m}$ are constructed. For our purposes, it is sufficient to say that $|h^{\rm insp-plunge}_{\ell m}|(t^{\ell m}_{\rm match})$, $\partial_t |h^{\rm insp-plunge}_{\ell m}(t^{\ell m}_{\rm match})|$, and $\omega^{\rm insp-plunge}_{\ell m}(t^{\ell m}_{\rm match})$ are the same as the NR values of

$$|h^{\rm NR}_{\ell m}|, \qquad \partial_t |h^{\rm NR}_{\ell m}|, \quad \text{and} \quad \omega^{\rm NR}_{\ell m},$$

at $t = t^{\ell m}_{\rm match}$. The values of these three quantities are obtained for each BBH, from the Simulating eXtreme Spacetimes (SXS) catalog of NR waveforms [85], after which a fitting formula that depends on the symmetric mass ratio ν and spins χ_1 and χ_2 is obtained to interpolate over the parameter space covered by the catalog. Their explicit forms can be found in Ref. [64], Appendix B. At this point, we are left with the free parameters $c^{\ell m}_{i,f}$ and $d^{\ell m}_{i,f}$ $(i = 1, 2)$ to fix. This is accomplished through fits against NR and Teukolsky equation-based waveforms [79,80], written also

as functions of ν, χ_1 and χ_2. The explicit form of these fits can be found in Ref. [64], Appendix C.

B. Construction of the parametrized model

With this framework established, our strategy to develop a parametrized SEOBNRHM model (hereafter pSEOBNRHM) is the following. We will introduce fractional deviations to the NR-informed formulas for the mode amplitudes and angular frequencies at $t = t^{\ell m}_{\rm match}$, i.e.,

$$|h^{\rm NR}_{\ell m}| \to |h^{\rm NR}_{\ell m}|(1+\delta A_{\ell m}), \tag{2.12a}$$

$$\omega^{\rm NR}_{\ell m} \to \omega^{\rm NR}_{\ell m}(1+\delta\omega_{\ell m}), \tag{2.12b}$$

and we will also allow for changes to $t^{\ell m}_{\rm match}$ by modifying the time-lag parameter $\Delta t^{\rm GR}_{\ell m}$ [defined in Eq. (2.6)] as

$$\Delta t^{\rm GR}_{\ell m} \to \Delta t^{\rm GR}_{\ell m}(1+\delta\Delta t_{\ell m}), \tag{2.13}$$

where we constrain $\delta\Delta t_{\ell m} > -1$ to ensure that $t^{\ell m}_{\rm match}$ remains less than $t^{\Omega}_{\rm peak}$, and thus before the end of the dynamics, as originally required [64,86]. Equations (2.12) and (2.13) modify the constrained parameters $c^{\ell m}_{i,c}$ and $d^{\ell m}_{i,c}$ through Eqs. (2.9) and (2.10), and consequently $\tilde{A}_{\ell m}$ and $\tilde{\phi}_{\ell m}$ that appear in the merger-ringdown waveform (2.7) and are given by Eq. (2.8). It is important to emphasize that Eqs. (2.12) and (2.13) also modify the NQC coefficients which enter the inspiral-plunge waveform in Eq. (2.11). This is because both $|h^{\rm NR}_{\ell m}|$ and $\omega^{\rm NR}_{\ell m}$ are used to fix some parameters in the explicit form of $N_{\ell m}$. We refer the reader to Refs. [63,87] and in particular to Ref. [64], Sec. III C, for details. Hence, although we will refer to $\delta A_{\ell m}$, $\delta\omega_{\ell m}$, and $\delta\Delta t_{\ell m}$ as "merger parameters" they, strictly speaking, also modify the plunge.

We also introduce non-GR deformations to the QNMs, following the same strategy applied in Refs. [33,34,39,40,43,88]. It consists in modifying the QNM oscillation frequency and damping time, defined respectively for the zero overtone $n = 0$, as

$$f_{\ell m0} = \frac{1}{2\pi}{\rm Re}(\sigma_{\ell m0}) = -\frac{1}{2\pi}\sigma^{\rm I}_{\ell m0}, \tag{2.14a}$$

$$\tau_{\ell m0} = -\frac{1}{{\rm Im}(\sigma_{\ell m0})} = -\frac{1}{\sigma^{\rm R}_{\ell m0}}, \tag{2.14b}$$

according to the substitutions

$$f_{\ell m0} \to f_{\ell m0}(1+\delta f_{\ell m0}), \tag{2.15a}$$

$$\tau_{\ell m0} \to \tau_{\ell m0}(1+\delta\tau_{\ell m0}), \tag{2.15b}$$

and we impose that $\delta\tau_{\ell m0} > -1$ to ensure that the remnant BH is stable (i.e., it rings downs, instead of "ringing-up" exponentially). Note that in Refs. [39,40], such deformations also concerned with the higher overtones, since the EOB model used for the merger-ringdown included higher overtones.

Put it all together, we have the following set of plunge-merger-ringdown parameters:

$$\begin{aligned}\boldsymbol{\vartheta}_{\rm nGR} &= \boldsymbol{\vartheta}^{\rm merger}_{\rm nGR} \cup \boldsymbol{\vartheta}^{\rm RD}_{\rm nGR} \\ &= \{\delta A_{\ell m}, \delta\omega_{\ell m}, \delta\Delta t_{\ell m}\} \cup \{\delta f_{\ell m0}, \delta\tau_{\ell m0}\},\end{aligned} \tag{2.16}$$

intended to capture possible signatures of beyond-GR physics in the most dynamical and nonlinear stage of a BBH coalescence. We will casually refer to them as "non-GR" or as "deformation" (away from GR) parameters. In Table I, we summarize the $\boldsymbol{\vartheta}_{\rm nGR}$ parameters, their meaning, and the constraints, if any, on their values. The GR limit is recovered when all parameters in $\boldsymbol{\vartheta}_{\rm nGR}$ are set to zero.

The pSEOBNRHM model allows us to change the non-GR plunge-merger parameters $\boldsymbol{\vartheta}^{\rm merger}_{\rm nGR}$ for each (ℓ, m) mode individually. Here, for a first study, we will assume that their values are the same across different modes, that is to say,

$$\delta A_{\ell m} = \delta A, \quad \delta\omega_{\ell m} = \delta\omega, \quad \text{and} \quad \delta\Delta t_{\ell m} = \delta\Delta t, \tag{2.17}$$

for all the ℓ and m modes in the waveform model. This choice is motivated by the fact that in GW150914 there are no significant changes in the posterior distributions of the binary parameters when using all the modes and only the $\ell = m = 2$ mode. As for the non-GR ringdown parameters $\boldsymbol{\vartheta}^{\rm RD}_{\rm nGR}$, we will assume that they are nonzero only for the least-damped ($n = 0$) (2, 2) mode. Under these assumptions, we have a 16-dimensional parameter space to work with,

TABLE I. Summary of the non-GR parameters in the pSEOBNRHM model. The ringdown deformation parameters $\delta f_{\ell m0}$ and $\delta\tau_{\ell m0}$ were introduced to the SEOBNRHM model in Ref. [40], while the merger deformation parameters $\delta A_{\ell m}$, $\delta\omega_{\ell m}$, and $\delta\Delta t_{\ell m}$ are introduced here for the first time. As explained in Sec. II B, although we call these merger parameters, they do also affect the late inspiral-plunge part of the waveform. We quote under the column labeled "bound" the constraints on the parameter's values required by our waveform model.

	Parameter	Deformation	Bound
Merger	$\delta A_{\ell m}$	Amplitude	
	$\delta\omega_{\ell m}$	Instantaneous frequency	
	$\delta\Delta t_{\ell m}$	Time lag	> -1
Ringdown	$\delta f_{\ell m0}$	Oscillation frequency	
	$\delta\tau_{\ell m0}$	Damping time	> -1

$$\boldsymbol{\vartheta} = \boldsymbol{\vartheta}_{\rm GR} \cup \boldsymbol{\vartheta}_{\rm nGR}, \tag{2.18}$$

where the GR parameters $\boldsymbol{\vartheta}_{\rm GR}$ are defined in Eq. (2.1).

Some comments follow in order. First, the parametrized deformation of SEOBNRHM we have introduced is not unique. For instance, we could have added additional fractional changes to $\partial_t |h^{\rm NR}_{\ell m}|(t^{\ell m}_{\rm match})$ or to the free parameters in the merger-ringdown waveform segment [see Eq. (2.8)]. We have found a compromise between the number of new parameters we can introduce and the physics we want to model; the optimal scenario being that of having the most flexible GW model that depends on the least number of deviation parameters. In our case, we find the parameters $\boldsymbol{\vartheta}_{\rm nGR}$ defined in Eq. (2.16) to be sufficient for our purposes. Second, one may fear that by effectively "undoing" the NR calibration we would obtain nonphysical GWs. This is not the case, as shown in Fig. 1 and as we will see in Sec. III. Our model produces waveforms that are smooth deformations of the ones of GR and have sufficient flexibility to be applied in tests of GR (Secs. V and VI) and provide a diagnostic tool for the presence of systematic effects in GR GW models (Sec. VII).

III. WAVEFORM MORPHOLOGY

Having introduced our waveform model, we now discuss how each of the parameters $\boldsymbol{\vartheta}^{\rm merger}_{\rm nGR}$ modify the GW signal in GR. An analogous exploration was done for $\boldsymbol{\vartheta}^{\rm RD}_{\rm nGR}$ in Ref. [40], for this reason the present discussion is restricted to the merger parameters. In each of the following sections, we vary the parameters δA, $\delta\omega$, and $\delta\Delta t$ one at a time. We take the binary component masses and spins to be

$$q = 0.867, \qquad \nu = 0.249, \qquad \chi_1 = \chi_2 = 0, \tag{3.1}$$

which are archetypal values of a GW150914-like event [15], the inclination to be $\iota = 0$ and, for clarity, we show results only for h_{22}. This is the dominant mode for such a quasicircular, nonspinning, and comparable-mass BBH. We end each section by showing how the waveform is modified when we apply the deformations, with the same values, simultaneously to all GW modes present in pSEOBNRHM.

A. The amplitude parameter δA

Let us start with δA, the amplitude parameter. In Fig. 2 we show the real part of $h_{22}(t)$, rescaled by the luminosity distance $D_{\rm L}$ and total mass M, for two values of δA: 0.5 (top panel) and -0.5 (bottom panel). The dashed segment corresponds to $t \leq t^{22}_{\rm match}$ (i.e., the inspiral-plunge part of waveform), whereas the solid segment corresponds to $t > t^{22}_{\rm match}$ (i.e., the merger-ringdown part of the waveform). In both panels, the black curve corresponds to the GR signal ($\delta A = 0$) with the same binary parameters. Both the GR and non-GR waveforms have been shifted in time and aligned in phase around 20 Hz following the prescription of Refs. [59,86,89,90]. The amplitudes of the non-GR waveforms $\pm|h_{22}|$ are shown by the dotted lines and form the envelope around $\mathrm{Re}(h_{22})$.

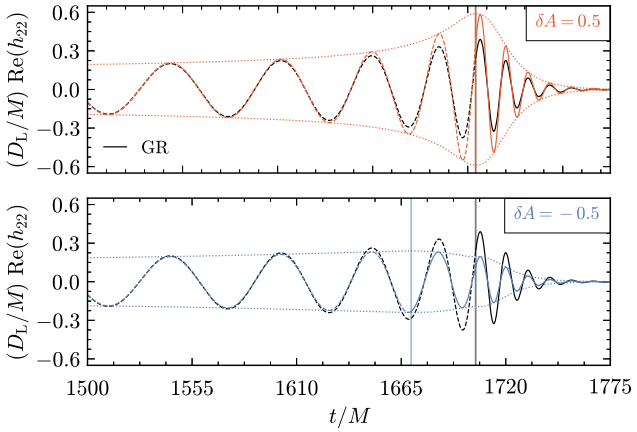

FIG. 2. The time evolution near the merger of the real part of the h_{22} mode for nonzero values of the amplitude parameter δA. We show the GR prediction ($\delta A = 0$) with the black lines. Top panel: for $\delta A = 0.5$. Bottom panel: for $\delta A = -0.5$. In both panels, we also show $\pm|h_{22}|$ for the non-GR waveform (dotted lines), and we use different line styles for the segment $t \leq t^{22}_{\rm match}$ (dashed lines) and $t > t^{22}_{\rm match}$ (solid lines) for all waveform illustrated. The matching times $t^{22}_{\rm match}$ are marked by the vertical lines.

Unsurprisingly, for positive values of δA, the amplitude $|h_{22}|$ increases relative to its GR value while keeping $t^{22}_{\rm match} \approx 1704M$ the same. The situation is more interesting for $\delta A < 0$. For the binary under consideration, we find that $|h_{22}|$ decreases for $\delta A \gtrsim -0.31$, but for $\delta A \lesssim -0.31$, we see that δA pinches downwards the amplitude enough to result in a local minimum (which we will refer to as $t^{22}_{\rm min}$) and two maxima, located before and after $t^{22}_{\rm min}$, with the global maximum happening at $t^{22}_{\rm max} < t^{22}_{\rm min}$. The values of both maxima are smaller than the GR peak amplitude. By construction, the matching time $t^{22}_{\rm match}$ is then shifted to earlier times relative to its GR value. For the example of $\delta A = -0.5$ shown in the bottom panel of Fig. 2, the matching time is at approximately $1670M$ (compare the location of the vertical lines in this panel).

In Fig. 3, we show a "continuum" of waveforms around the time of merger, obtained by finely covering the interval $\delta A \in [-0.5, 0.5]$, and including δA modifications to all modes in pSEOBNRHM. The GR prediction is shown by the black solid line. The top panel shows the real part of the strain, the middle panel the strain amplitude, and the bottom panel the instantaneous frequency, defined as $f = (2\pi)^{-1} \mathrm{d}\arg(h_+ - \mathrm{i}h_\times)/\mathrm{d}t$. As expected, we see that f does not change by varying δA, while the middle panel shows clearly how δA changes the GW amplitude. For negative values of δA, the presence of a local minimum in the GW amplitude is evident, as discussed previously.

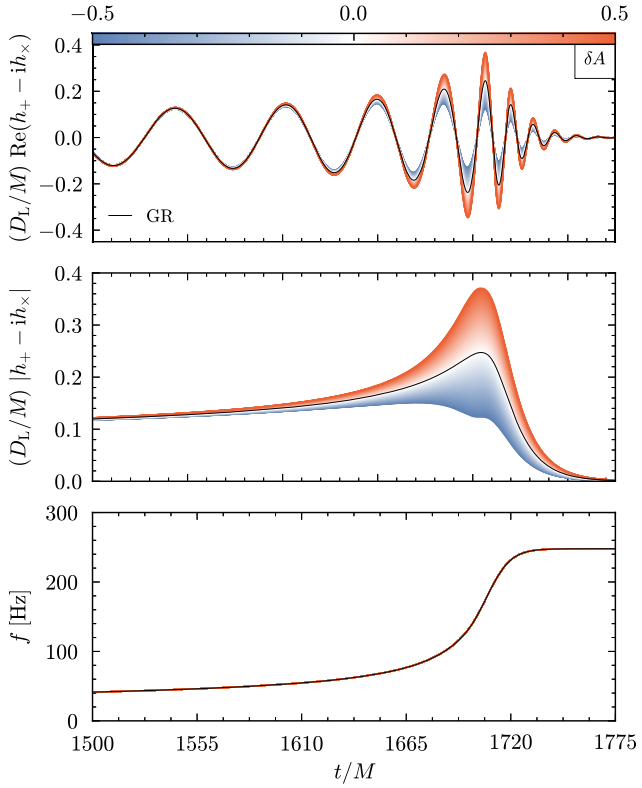

FIG. 3. The time evolution near the merger of the GW strain for nonzero values of the amplitude parameter δA, taken to affect in the same way all the $h_{\ell m}$ modes. The GR prediction ($\delta A = 0$) is shown by the black curves. We show the real part of the strain (top panel), the strain amplitude (middle panel), and the instantaneous frequency (bottom panel). As expected, the latter is unaffected by the changes to the peak amplitude of the various GW modes.

B. The frequency parameter $\delta\omega$

We now consider $\delta\omega$, the frequency parameter. Figure 4 is analogous to Fig. 2, except that we now consider $\delta\omega = 0.5$ (top panel) and $\delta\omega = -0.5$ (bottom panel). We see that $\delta\omega$ induces a time-dependent phase shift to the waveform, with its effects being most noticeable near the merger, and causing $t_{\rm match}$ to happen later (earlier) relative to GR when $\delta\omega > 0$ ($\delta\omega < 0$), while keeping the peak amplitude unaffected.

In Fig. 5, we show an analogous version of Fig. 3, but now for $\delta\omega$. Once more, the top panel shows the real part of the strain, the middle panel the strain amplitude, and the bottom panel the instantaneous frequency. We focus on the region near the merger and we plot the GR curves ($\delta\omega = 0$) with black solid lines. In the top panel, we can see the phase differences between the non-GR and GR waveforms, which are the largest around the time of merger and ringdown. This is in part due to the $\delta\omega$ itself, but also to the phase-shift and time-alignment procedure already mentioned, which we perform with respect to the GR waveform. The effect of the latter is small, as can be seen in the middle panel for the

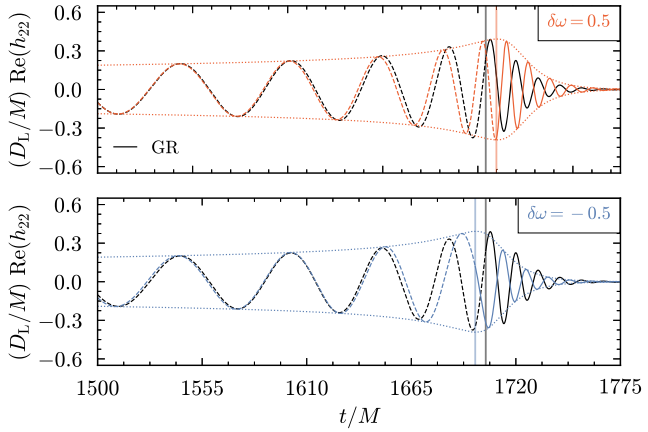

FIG. 4. The time evolution near the merger of the real part of the h_{22} mode for nonzero values of the frequency parameter $\delta\omega$. We show the GR prediction ($\delta\omega = 0$) with the black lines. Top panel: for $\delta\omega = 0.5$. Bottom panel: for $\delta\omega = -0.5$. In both panels, we also show $\pm|h_{22}|$ for the non-GR waveform (dotted lines), and we use different line styles for the segment $t \le t^{22}_{\rm match}$ (dashed lines) and $t > t^{22}_{\rm match}$ (solid lines) for all waveform illustrated. The matching times $t^{22}_{\rm match}$ are marked by the vertical lines.

amplitude, where all curves nearly overlap in time. In the bottom panel, we note sharp changes to f when $|\delta\omega| \approx 0.5$. They originate from us not imposing the continuity of the time derivative of $\omega^{\rm NR}_{\ell m}$ at $t = t^{\ell m}_{\rm match}$ [63,64].

C. The time shift parameter $\delta\Delta t$

Finally, we now consider $\delta\Delta t$, the time shift parameter. In Fig 6, which is analogous to both Figs. 2 and 4, we show waveforms for $\delta\Delta t = 0.5$ (top panel) and $\delta\Delta t = -0.5$ (bottom panel). Overall, we see small changes to the GR waveform, in the form of an earlier $t_{\rm match}$ when $\delta\Delta t > 0$, and later $t_{\rm match}$ when $\delta\Delta t < 0$. Here, the changes due to the phase-shift and time-alignment are negligible, and the shifts seen in the figure are due to $\delta\Delta t$.

Finally, in Fig. 7 we show a sequence of waveforms around the time of merger, obtained by finely covering the interval $\delta\Delta t \in [-0.5, 0.5]$. The GR prediction is shown by the black solid line. We see that the changes to the strain (top panel), its amplitude (middle panel), and its frequency evolution (bottom panel) are small. Therefore, $\delta\Delta t$ introduces changes to the GR waveform which are in general subdominant relative to those due to δA and $\delta\omega$. We also remark that $\Delta t^{\rm GR}_{\ell m}$ is not very sensitive to the EOB calibration against NR waveform. Hence, the fractional changes we are introducing on $\Delta t^{\rm GR}_{\ell m}$ are comparable with the NR fitting errors. This explains why this parameter affects the GR waveforms so little.

IV. PARAMETER ESTIMATION

In the previous section, we have introduced our waveform model and discussed the properties of the waveform

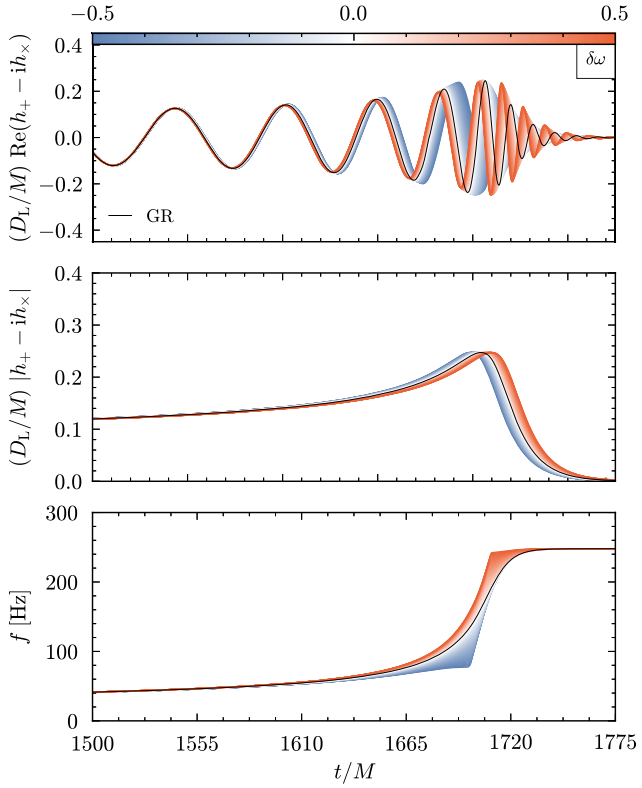

FIG. 5. The time evolution near the merger of the GW strain for nonzero values of the frequency parameter $\delta\omega$, assumed to be the same for all $h_{\ell m}$ modes. The GR prediction ($\delta\omega = 0$) is shown by the black curves. We show the real part of the strain (top panel), the strain amplitude (middle panel), and the instantaneous frequency (bottom panel). In the top panel, we clearly see the phase difference between the non-GR and GR waveform near the merger. This is partially due to the $\delta\omega$ itself, but also to the phase-shift and time-alignment done with respect to the GR waveform. The effect of the latter is small as can be seen in the middle panel, which shows the amplitude. The sharp changes to f in the bottom panel for $|\delta\omega| \approx 0.5$ originate from us not imposing the continuity of the time derivative of $\omega^{\mathrm{NR}}_{\ell m}$ at $t = t^{\ell m}_{\mathrm{match}}$.

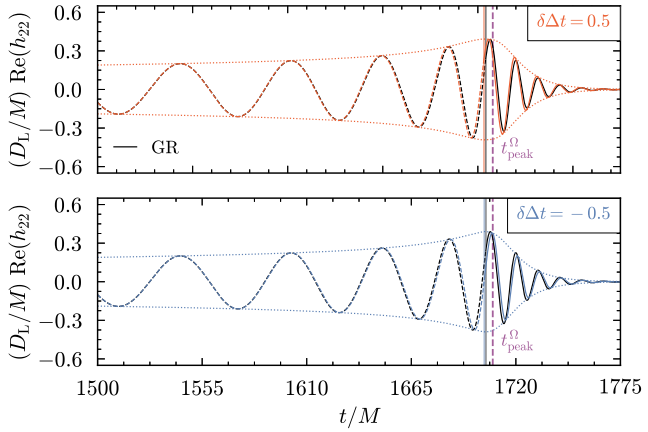

FIG. 6. The time evolution near the merger of the real part of the h_{22} mode for nonzero values of the time shift parameter $\delta\Delta t$. We show the GR prediction ($\delta\Delta t = 0$) with the black lines. Top panel: for $\delta\Delta t = 0.5$. Bottom panel: for $\delta\Delta t = -0.5$. In both panels, we also show $\pm|h_{22}|$ for the non-GR waveform (dotted lines), and we use different line styles for the segment $t \le t^{22}_{\mathrm{match}}$ (dashed lines) and $t > t^{22}_{\mathrm{match}}$ (solid lines) for all waveform illustrated. The matching times t^{22}_{match} are marked by the vertical lines. For reference, we also show the instant in which the EOB frequency peaks ($t^{\Omega}_{\mathrm{peak}}$) with vertical dashed lines.

morphology. Here, we summarize the Bayesian inference formalism used for parameter estimation of GW signals and synthetic-data studies. We describe the prior choices and the criteria for the GW event selection.

A. Bayesian parameter estimation

Our hypothesis, $\mathcal{H}$, is that in the detector data, d, an observed GW signal is described by the waveform model `pSEOBNRHM`. The model `pSEOBNRHM` has a set of GR and non-GR parameters, as in Eqs. (2.1) and (2.16), where

$$\boldsymbol{\vartheta}_{\mathrm{nGR}} = \{\delta A, \delta\omega, \delta\Delta t, \delta f_{220}, \delta\tau_{220}\}. \tag{4.1}$$

As said, we assume that the merger modifications are the same for all (ℓ, m) modes present in the model `pSEOBNRHM`.

The posterior probability distribution on the parameters of the model, $\boldsymbol{\vartheta}$, given the hypothesis, $\mathcal{H}$, is obtained using Bayes' theorem,

$$P(\boldsymbol{\vartheta}|d,\mathcal{H}) = \frac{P(\boldsymbol{\vartheta}|\mathcal{H})P(d|\boldsymbol{\vartheta},\mathcal{H})}{P(d|\mathcal{H})}, \tag{4.2}$$

where $P(\boldsymbol{\vartheta}|\mathcal{H})$ is the prior probability distribution, $P(d|\boldsymbol{\vartheta},\mathcal{H})$ is the likelihood function, and $P(d|\mathcal{H})$ is the evidence of the hypothesis $\mathcal{H}$. For a detector with stationary, Gaussian noise and power spectral density $S_n(f)$, the likelihood function can be written as

$$P(d|\boldsymbol{\vartheta},\mathcal{H}) \propto \exp\left[-\frac{1}{2}\langle d - h(\boldsymbol{\vartheta})|d - h(\boldsymbol{\vartheta})\rangle\right], \tag{4.3}$$

where the noise-weighted inner product is defined as

$$\langle A|B\rangle = 2\int_{f_{\mathrm{low}}}^{f_{\mathrm{high}}} \mathrm{d}f\, \frac{\tilde{A}^*(f)\tilde{B}(f) + \tilde{A}(f)\tilde{B}^*(f)}{S_n(f)}, \tag{4.4}$$

where $\tilde{A}(f)$ is the Fourier transform of $A(t)$, and the asterisk denotes the complex conjugation, and $S_n(f)$ is the one-sided power spectral density of the detector. The integration limits f_{low} and f_{high} set the bandwidth of the detector's sensitivity. We follow the LVK analysis and set $f_{\mathrm{low}} = 20$ Hz, while f_{high} is the Nyquist frequency [19]. The posterior distributions are computed by using `LALInferenceMCMC` [91,92], a Markov-chain Monte Carlo that uses the Metropolis-Hastings algorithm to survey the

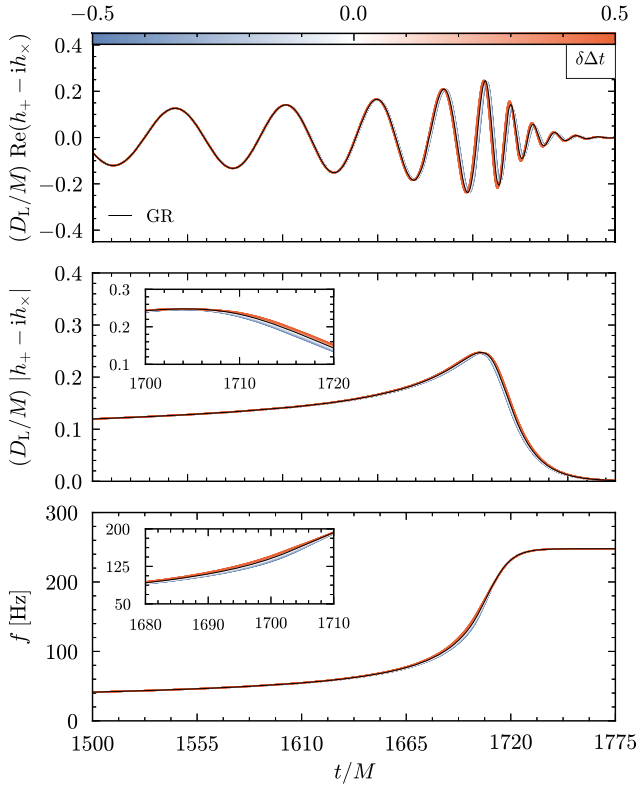

FIG. 7. The time evolution near the merger of the GW strain for nonzero values of the time shift parameter $\delta\Delta t$, assumed to be the same for all $h_{\ell m}$ modes. The GR prediction ($\delta\Delta t = 0$) is shown by the black curves. We show the real part of the strain (top panel), the strain amplitude (middle panel), and the instantaneous frequency (bottom panel). The insets zoom into the time intervals $t/M \in [1700, 1720]$ in the middle panel and $t/M \in [1500, 1775]$ in the bottom panel.

likelihood surface and is implemented in LALInference [93], part of the LALSuite software suite [94].

B. Prior choices

The prior distributions on the GR parameters are assumed to be uniform in the component masses (m_1, m_2), uniform and isotropic in the spin magnitudes (χ_1, χ_2), isotropic on the binary orientation, and isotropically distributed on a sphere for the source location with $P(D_L) \propto D_L^2$.

For the non-GR parameters, as explained in Sec. II B, the internal consistency of the pSEOBNRHM model requires that both $\delta\Delta t$ and $\delta\tau_{220}$ are larger than -1 (cf. Table I). We use this fact to fix a common lower limit on the uniform priors on all $\boldsymbol{\vartheta}_{\rm nGR}$. We set 1 to be an upper limit on the uniform priors on the non-GR parameters. This was sufficient in most of our analysis, but in a few cases we found that the marginalized posteriors distributions for one or more non-GR parameters had support at $\boldsymbol{\vartheta}_{\rm nGR} \approx 1$. In such cases we extended the priors' domains to $\boldsymbol{\vartheta}_{\rm nGR} \in (-1, +2]$. Even at this wider range, we did not find anomalies in the waveform.

C. Event selection

The pSEOBNRHM ringdown analysis performed in Ref. [13] selected GW events from the GWTC-3 catalog [19] which had a signal-to-noise ratio (SNR) ≥ 8 in the inspiral and post-inspiral regimes. The requirement on the inspiral regime allows one to break the strong degeneracy between the total mass of the binary and the ringdown deviation parameters [39,40]. Among the GW events that meet this criteria, two stand out in terms of their constraining power on $\boldsymbol{\vartheta}^{\rm RD}_{\rm nGR}$, namely GW150914 [14,15] and GW200129_065458 (hereafter GW200129) [19]. These two events, with a median total source-frame masses of $64.5M_\odot$ and $63.4M_\odot$, respectively, are among the loudest BBH signals to date with a median total network SNR of 26.0 and 26.8, respectively [18,19]. GW150914 was detected by the two LIGO detectors at Hanford and Livingston, whereas GW200129 was detected by the three-detector network of LIGO Hanford, Livingston, and Virgo.

We guide ourselves by this result and use these two events to investigate what constraints we can place on the merger-ringdown parameters. We remark that this SNR selection criteria may be too strong if we are interested in $\boldsymbol{\vartheta}^{\rm merger}_{\rm nGR}$ only. We leave the study of the optimal SNR to constrain only the merger parameters to a future work.

V. RESULTS: SYNTHETIC-SIGNAL INJECTION STUDIES

In this section, we use pSEOBNRHM to perform a number of synthetic-signal injection studies. As we saw in Sec. II, pSEOBNRHM is a smooth deformation of the GR waveform model SEOBNRHM, which is recovered when all $\boldsymbol{\vartheta}_{\rm nGR}$ parameters are set to zero. This allows us to explore different scenarios that differ from one another on whether the GW signal and the GW model used to infer the parameters of this signal are described by GR ($\boldsymbol{\vartheta}_{\rm nGR} = 0$) or not ($\boldsymbol{\vartheta}_{\rm nGR} \neq 0$). We summarize these possibilities in Table III.

To prepare the GW signal we need to fix $\boldsymbol{\vartheta} = \boldsymbol{\vartheta}_{\rm GR} \cup \boldsymbol{\vartheta}_{\rm nGR}$. In all cases, we use values of $\boldsymbol{\vartheta}_{\rm GR}$ illustrative of a GW150914-like BBH as in Table II. We set all non-GR parameters to the same value, $\boldsymbol{\vartheta}_{\rm nGR} = 0.1$, whenever the injected signal is non-GR. By working exclusively with the pSEOBNRHM waveform model, we avoid introducing systematic errors due to waveform modeling in our analysis. We also employ an averaged (zero-noise) realization of the noise to avoid statistical errors due to noise. The resulting GW signal is then analyzed with the power spectral density $S_n(f)$ of the LIGO Hanford and Livingston detectors both at design sensitivity [95]. In all cases, we set the distance to the binary to be such that the total network SNR is approximately 100.

In Sec. V A, we do a preliminary analysis where both injected and model waveforms are described by GR. This allows us to access the accuracy with which different binary parameters can be recovered from the data in the detector

TABLE II. Values of the parameters $\vartheta_{\rm GR}$ used in all synthetic-signal injection studies in Sec. V. The parameters are representative of GW150914, except for the luminosity distance, which is chosen such that the total SNR, in a detector network constituted by LIGO Hanford and Livingston operating at design sensitivity, is approximately 100.

Parameter (detector frame)	Value
Primary mass, m_1 $[M_\odot]$	38.5
Secondary mass, m_2 $[M_\odot]$	33.4
Primary spin, χ_1	3.47×10^{-3}
Secondary spin, χ_2	-4.40×10^{-2}
Inclination, ι [rad]	2.69
Polarization, ψ [rad]	1.58
Right ascension, α [rad]	1.22
Declination, δ [rad]	−1.46
Luminosity distance, $D_{\rm L}$ [Mpc]	337
Reference time, t_c [GPS]	1126285216
Reference phase, ϕ_c [rad]	0.00

TABLE III. Summary of the synthetic-signal injection simulations performed in Sec. V. The label "GR" refers to the SEOBNRHM waveform model, whereas the label "non-GR" refers to the pSEOBNRHM waveform model, where all merger-ringdown parameters are set deviate in 10% deviations relative to their corresponding GR values.

		Model	
		GR	non-GR
Injection	GR	Section V A	Section V B
	non-GR	Section V A	Section V C

network. With these results as a benchmark, we can then proceed to inject a non-GR waveform and analyze it with a GR model. This allows us to study the systematic error introduced on the inferred binary parameters by assuming *a priori* that GR is true, while nature may not be so (the so-called fundamental bias). In Sec. V B, we inject a GR waveform and try to recover its parameters with a non-GR model. This allows us to answer how much the non-GR parameters can be constrained given an event consistent with GR. Finally, in Sec. V C, we use non-GR waveforms as both our injection and our model. This answers whether we can detect the presence of the non-GR parameters in our signal.

A. Fundamental biases on binary parameters

We first explore the presence (or not) of biases in the inference of binary parameters when the template waveform model assumes GR, while the injected GW signal is non-GR [31,96]. For this purpose, we first inject a synthetic GR GW signal with SNR = 98 and recover the binary parameters with a GR model. By doing this exercise first, we gain an idea on the accuracy with which the parameters of the binary (cf. Table II) can be recovered in our set up. Next, we repeat the same analysis but now using as our synthetic GW signal the one obtained with pSEOBNRHM. The signal is prepared using the same binary parameters $\vartheta_{\rm GR}$ shown in Table II with SNR = 104, but now we let $\vartheta_{\rm nGR} = 0.1$.

The results of our two analyses are shown in Fig. 8. We show the one- and two-dimensional posterior distributions of a subset of the intrinsic binary parameters, namely, the mass ratio q, the detector-frame chirp mass $\mathcal{M}$ and the effective spin $\chi_{\rm eff}$. In all panels, the "true" (injection) values of these parameters are marked by the vertical and horizon lines. We see that in the case of a non-GR injection (solid curves), the posterior distributions of the parameters are shifted from the injected values and from the posterior distributions in the case of a GR injection (dashed curves). We attribute the differences in the 90% contours of the posterior distributions to the fact that in the non-GR injection a smaller value of the chirp mass $\mathcal{M}$ is inferred. This suggests that the GR waveform that best fits the data has a longer inspiral and this makes the inference of the other binary parameters more precise. The recovered SNR from the GR analysis of the non-GR signal is almost the same as the injected one, i.e., SNR = 104. Hence, if a GW signal with deviations from GR would be analyzed by

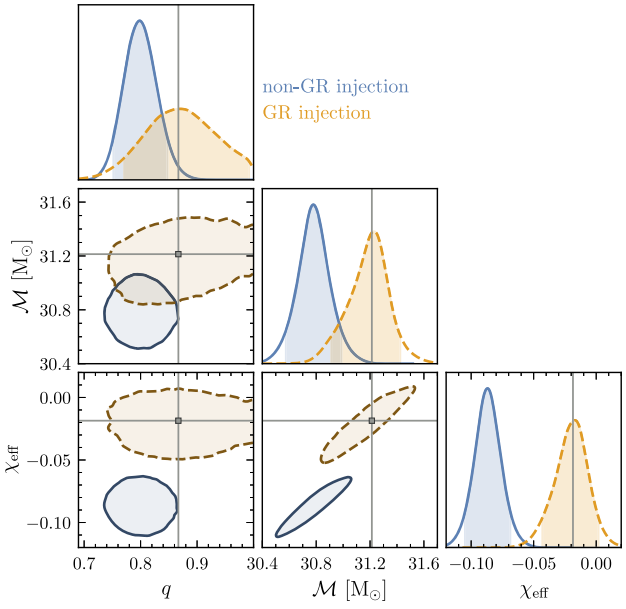

FIG. 8. The one- and two-dimensional posterior distributions on the intrinsic binary parameters of mass ratio q, detector-frame chirp mass $\mathcal{M}$ and effective spin $\chi_{\rm eff}$ for a GR injection (dashed curve) and a non-GR injection (solid curve) with 10% deviations in the merger-ringdown parameters $\vartheta_{\rm nGR}$. All contours indicate 90% credible regions. The parameter estimation is performed assuming the GR SEOBNRHM waveform model. The vertical and horizontal lines mark the injected values. The measurements with non-GR injections are visibly biased, most preeminently in $\chi_{\rm eff}$ and $\mathcal{M}$.

current GR templates, the GW event would be interpreted as a BBH in GR with different values of the binary parameters.

B. Constraints on deviations to general relativity

We now inject a synthetic GW signal in GR using the parameters $\boldsymbol{\vartheta}_{\rm GR}$ in Table II with SNR $= 98$. We analyze the signal using the pSEOBNRHM waveform model, allowing both $\boldsymbol{\vartheta}_{\rm GR}$ in Eq. (2.1) and $\boldsymbol{\vartheta}_{\rm nGR}$ in Eq. (4.1) to vary. This simulates a scenario where we have a GW event consistent with GR and we want to understand which constraints it places on the non-GR parameters in our waveform model.

We summarize the results of the analysis in Fig. 9, where we show the one- and two-dimensional posterior probability distributions of the merger-ringdown parameters $\boldsymbol{\vartheta}_{\rm nGR}$. We find that the marginalized posterior distributions of the non-GR parameters are consistent with the corresponding injected values in GR, which are indicated by the markers. We can infer that a GW150914-like event with SNR $= 98$ would constrain the deformation parameters in the range between 5% (for δA and δf_{220}) and 20% (for $\delta\tau_{220}$) at 90% credible level. In the Appendix, Fig. 15, we show the posterior distributions on the intrinsic binary parameters.

The best constrained parameter is the amplitude, δA, whereas the less constrained parameter is the time shift, $\delta\Delta t$. For the latter, we obtain a posterior distribution that has support onto a wide range of the prior. This is perhaps unsurprising due to the small deviations caused by $\delta\Delta t$ in the waveform in comparison with $\delta\omega$ (compare Figs. 4 and 6). We also observe a negative correlation between these two parameters and hence increasing precision on one is likely to increase uncertainty on the other; see the $\delta\Delta t$–$\delta\omega$ panel in Fig. 9. Together, these results suggest that considering δA and $\delta\omega$ is sufficient, if one is interested in doing a test of GR only in the plunge-merger stage of the binary's coalescence.

C. Detecting deviations from general relativity

We now study whether we can detect the presence of the non-GR parameters. To do so, we inject a synthetic GW signal where the binary parameters are shown in Table II, SNR $= 104$, and we set the merger-ringdown parameters to be 10% larger than their corresponding GR values.

We summarize the outcome of our parameter estimation in Fig. 10, where we show the one- and two-dimensional posterior distributions for the $\boldsymbol{\vartheta}_{\rm nGR}$ parameters. We see that all posteriors are consistent with the injected values, indicated by the markers. Moreover, the posteriors for $\boldsymbol{\vartheta}_{\rm nGR}$ have support at their null, GR value. The exceptions are the amplitude δA and the QNM frequency δf_{220}

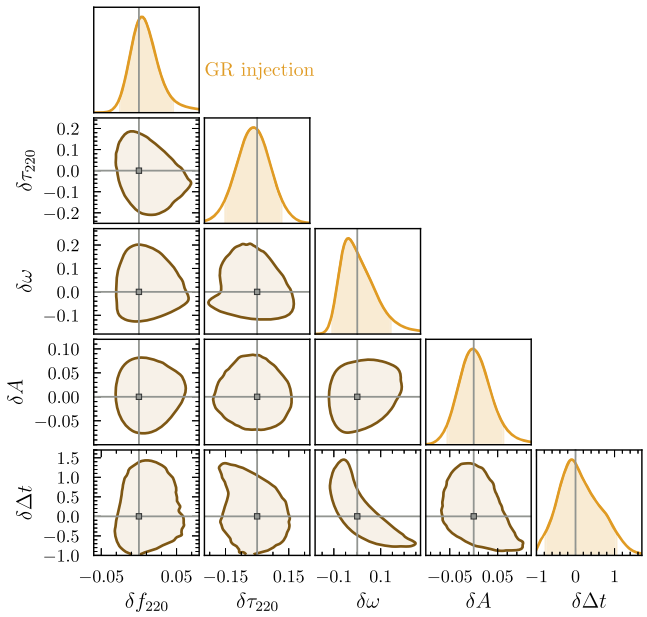

FIG. 9. The one- and two-dimensional posterior distributions on the merger-ringdown parameters $\boldsymbol{\vartheta}_{\rm nGR}$. All contours indicate 90% credible regions. We considered a GR injection and recovered with the pSEOBNRHM model. The vertical and horizontal lines mark the injected values for the deviation parameters, i.e., $\boldsymbol{\vartheta}_{\rm nGR} = 0$. The inferred values on $\boldsymbol{\vartheta}_{\rm nGR}$ are consistent with the zero, and their width of the marginalized posterior distribution inform us with which accuracy we may constrain these parameters.

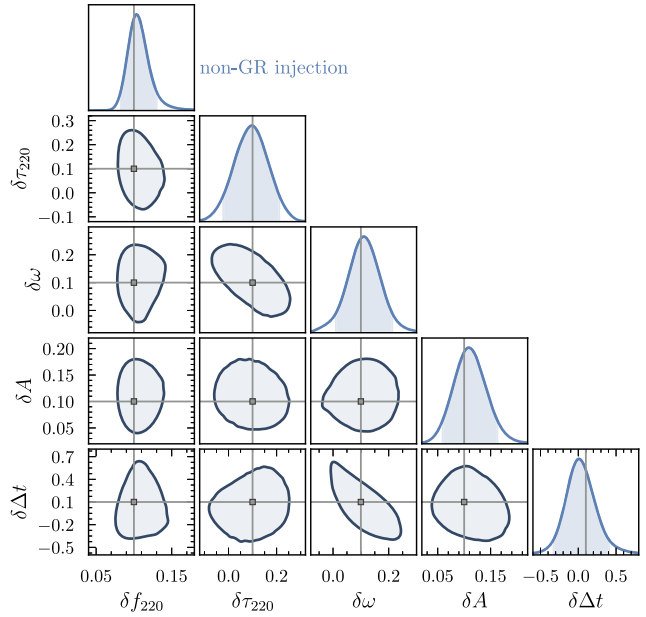

FIG. 10. The one- and two-dimensional posterior distributions on the merger-ringdown parameters $\boldsymbol{\vartheta}_{\rm nGR}$. All contours correspond to 90% credible regions. In comparison to Fig. 9, this time we use pSEOBNRHM prepare the injection. This allow us to understand how well we can measure the non-GR parameters. The vertical and horizontal lines mark the injected values for the deviation parameters, i.e., $\boldsymbol{\vartheta}_{\rm nGR} = 0.1$. The marginalized posterior distributions on $\boldsymbol{\vartheta}_{\rm nGR}$ are consistent with their injection values.

parameters, which have no support at their GR values at 90% credible level. This suggests that these two parameters are the most promising ones in signaling the presence of beyond-GR physics for GW150914-like binaries. In fact, we will see this suggestion taking place in our analysis of GW200129 in Sec. VII.

VI. ANALYSIS OF GW150914: CONSTRAINTS ON THE PLUNGE-MERGER-RINGDOWN PARAMETERS

Having gained some intuition on the role of the merger-ringdown parameters in the synthetic-signal injections presented in Sec. V, we now apply the `pSEOBNRHM` model to the analysis of real GW events. Our analysis, here and in Sec. VII, uses the power spectral density of the detectors from the Gravitational Wave Open Science Center (GWOSC) [97], and calibration envelopes as used for the analyses in Ref. [13]. We will start with GW1501914, the first GW event observed by the LIGO-Virgo Collaboration [14].

We will focus our analysis to two subsets of merger-ringdown parameters due to the smaller SNR of this event (and of GW200129) in comparison to the SNR ≈ 100 scenarios studied in the previous section. First, we have seen that the time-shift parameter $\delta\Delta t$ is the hardest parameter to constrain, and that it has wide posteriors even at such large SNRs. This motivates us to consider, among the merger parameters, only

$$\boldsymbol{\vartheta}_{\rm nGR} = \{\delta A, \delta\omega\}, \tag{6.1}$$

to perform a "merger test of GR." Second, we performed a parameter estimation of GW150914, using all $\boldsymbol{\vartheta}_{\rm nGR}$ parameters in Eq. (4.1). We found correlations between the frequency parameter $\delta\omega$ and the QNM deformations parameters δf_{220} and $\delta\tau_{220}$. Moreover, we also did a series of synthetic-signal injection studies using the binary parameters listed in Table II, with SNR $= 26$, and in Gaussian noise. In some of these cases, we also found correlations between $\delta\omega$ and δf_{220} and $\delta\tau_{220}$. In summary, these correlations arise either when the GW event has low SNR or due to noise. This suggests using

$$\boldsymbol{\vartheta}_{\rm nGR} = \{\delta A, \delta f_{220}, \delta\tau_{220}\}, \tag{6.2}$$

to perform a "merger-ringdown test of GR."

In Fig. 11 we show the results of our merger test of GR. The corner plot shows the one- and two-dimensional posterior probability distributions of δA and $\delta\omega$. The posterior distributions are consistent with the null value predicted in GR. We obtain from GW150914,

$$\delta A = -0.01^{+0.27}_{-0.19}, \quad \text{and} \quad \delta\omega = 0.00^{+0.17}_{-0.12}, \tag{6.3}$$

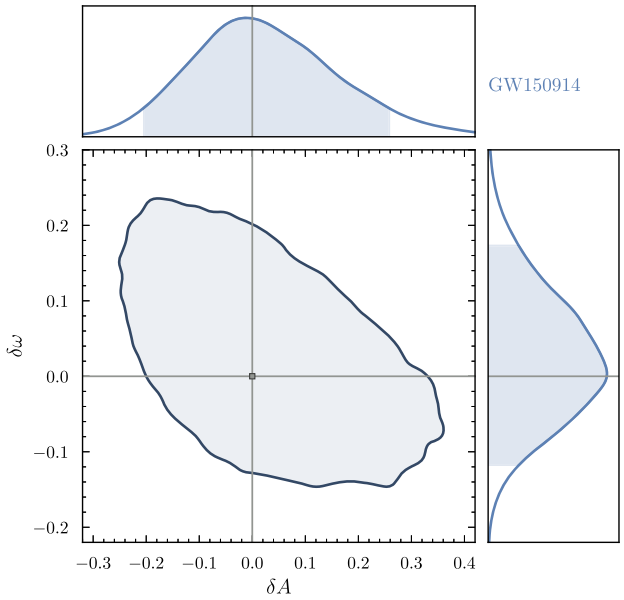

FIG. 11. The one- and two-dimensional posterior distributions on δA and $\delta\omega$ obtained by analyzing GW150914. All contours correspond to 90% credible regions. The marginalized posterior distributions are consistent with GR, i.e., $\delta A = \delta\omega = 0$, identified in the plot with the horizontal and vertical lines. We found that $\delta A = -0.01^{+0.27}_{-0.19}$ and $\delta\omega = 0.00^{+0.17}_{-0.12}$ at 90% credible level.

at 90% credible level. This shows that we can already constrain deviations from GR around the merger time of BBH coalescences to about 20% with present GW events.

Figure 12 is a similar plot, but for the merger-ringdown test of GR. Once more, we find that the inferred values of the non-GR parameters are consistent with GR,

$$\delta A = 0.03^{+0.29}_{-0.20}, \quad \delta f_{220} = 0.041^{+0.151}_{-0.084}, \quad \delta\tau_{220} = 0.04^{+0.27}_{-0.29}, \tag{6.4}$$

at 90% credible level. The bound on the amplitude parameter is similar to the one obtained in the merger test shown in Eq. (6.3). Also, the bounds on the ringdown parameters are similar to those obtain in Ref. [40] ($\delta f_{220} = 0.05^{+0.11}_{-0.07}$ and $\delta\tau_{220} = -0.07^{+0.26}_{-0.23}$), which had only these two quantities as its non-GR parameters. In the Appendix, Fig. 16, we show the posterior distributions on the intrinsic binary parameters for both tests of GR.

When interpreting our inferences on these parameters, it is important to note that the statistical error in our analysis ($\approx$20%) is larger than the systematic error due to fitting $|h^{\rm NR}_{\ell m}|$ and $\omega^{\rm NR}_{\ell m}$ against NR data, which is at most around 4% with current models [63,64], depending on where one is in the η–$\chi_{\rm eff}$ parameter space. In fact, we see that the median values of δA and $\delta\omega$ fall within this fitting error. In conclusion, we can claim to have placed a constraint on these non-GR parameters with GW150914.

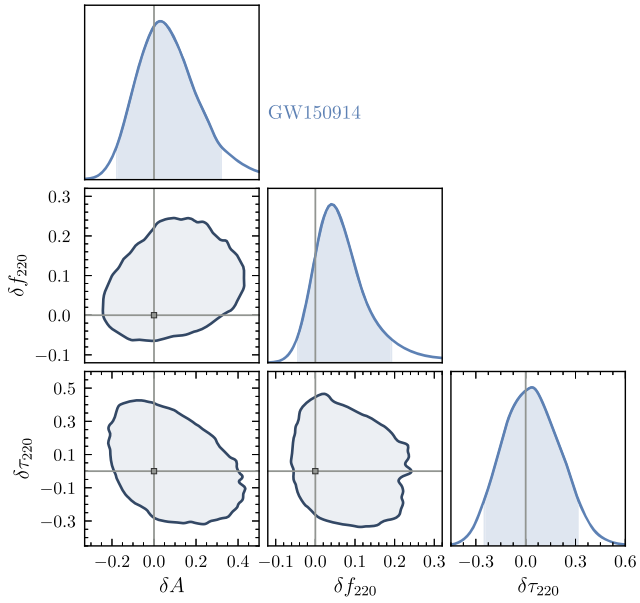

FIG. 12. The one- and two-dimensional posterior distributions on the merger parameter δA, and ringdown parameters δf_{220} and $\delta\tau_{220}$, obtained by analyzing GW150914. The marginalized posterior distributions are consistent with GR, i.e., $\delta A = \delta f_{220} = \delta\omega_{220} = 0$, identified in the plot with the horizontal and vertical lines. We found that GW150914 constrains these parameters to be $\delta A = 0.03^{+0.29}_{-0.20}$, $\delta f_{220} = 0.041^{+0.151}_{-0.084}$, and $\delta\tau_{220} = 0.04^{+0.27}_{-0.29}$ at 90% credible level.

VII. THE CASE OF GW200129: THE IMPORTANCE OF WAVEFORM SYSTEMATICS AND DATA-QUALITY IN TESTS OF GENERAL RELATIVITY

We now turn our attention to GW200129 and, following what we have learned in the previous section, we first consider pSEOBNRHM with only δA and $\delta\omega$ as non-GR parameters. We show the one- and two-dimensional marginalized posteriors of these parameters with the black solid curves in the left panel of Fig. 13. We see that while our inferred value of $\delta\omega$ ($\delta\omega = -0.002^{+0.097}_{-0.082}$ at the 90% credible level) is consistent with GR, our inferred value of δA ($\delta A = 0.44^{+0.38}_{-0.28}$ at the 90% credible level) exhibits a gross violation of GR.

Have we found a strong evidence of violation of GR in GW200129? Assuming that this is not the case, the apparent violation of GR could be either due to statistical errors or to systematic errors. To explore the first possibility, we perform a series of synthetic-data injection studies. As our first step, we do a parameter-estimation study in zero noise, where the injected GW signal is generated with SEOBNRHM and we use the binary parameters corresponding to the maximum likelihood point from the GWTC-3 data release by the LVK [98] analysis of GW200129. The LVK analysis was done separately with two quasicircular and spin-precessing waveform

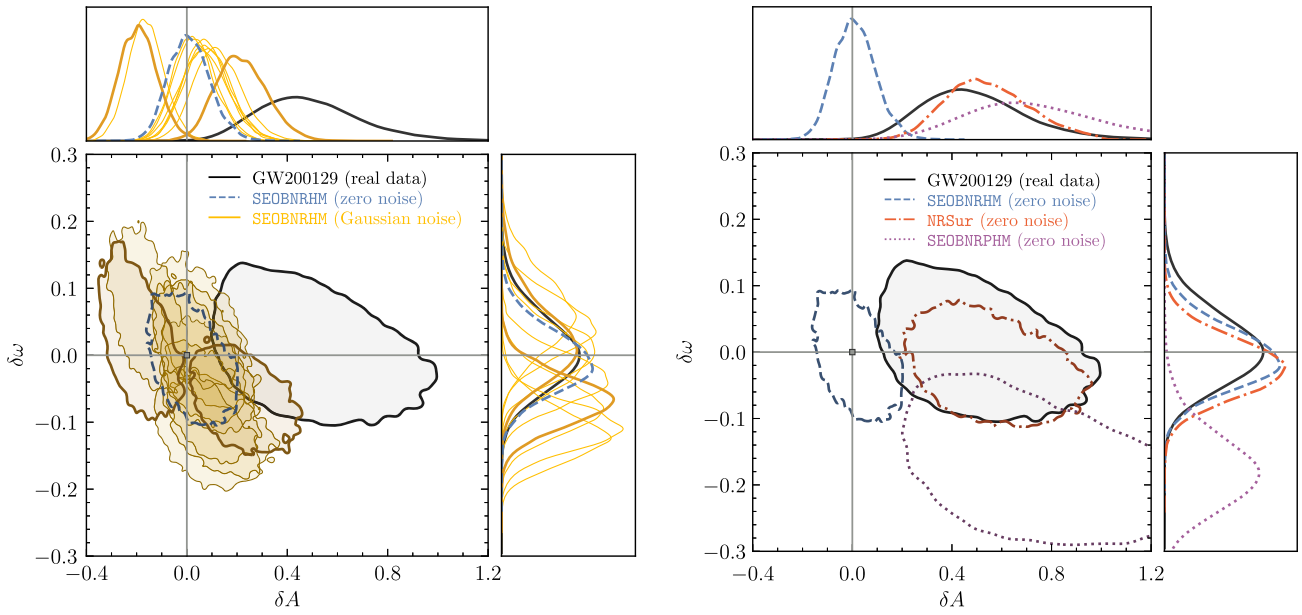

FIG. 13. Corner plots showing the one- and two-dimensional posterior distribution functions for δA and $\delta\omega$ for our studies of GW200129 and GW200129-like BBHs. All contours indicate 90% credible regions. Left panel: results of our reanalysis of GW200129 data with pSEOBNRHM (black solid curves) and for a GW200129-like injection generated with SEOBNRHM. For the latter, we used the maximum-likelihood point of LVK's original analysis of GW200129 which employed the IMRPhenomXPHM model to generate the synthetic GW signal. We performed the parameter estimation of these injections in zero noise (dashed curves) and in ten Gaussian noise realizations (yellow solid curves). Right panel: Similar, but having generated two additional GW200129-like synthetic signals with NRSur7dq4 (dot-dashed curves) and with SEOBNRv4PHM (dotted curves). Both models include spin-precession effects. Observe how the posteriors distributions are in tension with GR [marker at $(\delta A, \delta\omega) = (0, 0)$] when we include spin-precession effects in the synthetic data and we recover with a nonprecessing and non-GR waveform model.

models, SEOBNRv4PHM [65] and IMRPhenomXPHM [99], employing different parameter estimation libraries, RIFT [100–102] and Bilby [103,104], respectively. Here, as a reference, we use the maximum likelihood point of the analysis that employed the IMRPhenomXPHM model, and we expect the results to be qualitatively similar had we used SEOBNRv4PHM. More specifically, because the SEOBNRHM model we are using is nonprecessing, we use only the masses and luminosity distance from the maximum-likelihood point.

The resultant posterior distributions are shown in the left panel of Fig. 13 (dashed curves) and they are, reassuringly, consistent with GR. We also repeat this analysis for ten Gaussian noise realizations, using the same synthetic GW signal (yellow solid curves in the left panel of Fig. 13). Consistent with the expectations, two noise realizations yield marginalized posteriors on $\delta\omega$ and δA which are not consistent with GR at 90% credible level (shown by the thicker yellow solid curves). It is worth observing how the Gaussian noise curves have qualitatively the same shapes (spreads), with the two outliers being shifted away from $(\delta A, \delta\omega) = (0, 0)$. This is an expected behavior consistent with the stationary, Gaussian assumption of statistical noise. These results, hence, disfavor the possibility that the violations of GR we are observing are due to Gaussian noise or due to the particular binary parameters inferred for this event. The latter alternative would have been quite unlikely in the first place, because both GW200129 and GW150914 have similar binary parameters and SNRs, and we have already found that GW1501914 is consistent with GR in Sec. VI (cf. Fig. 11).

As our next step, we perform two additional parameter estimation runs, in zero noise, but now generating our synthetic GW signal with the SEOBNRv4PHM [65] and the NRSur7dq4 [105,106] waveform models. Both models allow for spin precession, unlike our pSEOBNRHM. Hence, we can study if the GR deviations we are finding are due to systematic errors in the GW modeling. Once again, the maximum-likelihood point of the LVK analysis of GW200129 using IMRPhenomXPHM was used, but this time with the binary in-plane spin components included. We show our results in the right panel of Fig. 13. The one- and two-dimensional posterior distributions of $\delta\omega$ and δA are shown in dash-dotted curves for the NRSur7dq4 injection and with dotted curves for the SEOBNRv4PHM injection. For reference, we also include the posterior distribution associated to the SEOBNRHM injection (dashed curves) and to the data from GW200129 (solid curves). We see that these two spin-precessing GW signals, when analyzed in zero noise, are also in disagreement with GR, when analyzed with our nonprecessing non-GR model. We also see that our results using NRSur7dq4 (which compares the best against NR simulations in its regime of validity) are in good agreement with what we obtain by analyzing the GW200129 data. These results, compared with those obtained from the SEOBNRHM injection, suggest that the presence of spin precession in the GR signal biases us to find a false evidence for beyond-GR effects when we use a nonprecessing non-GR model.

Is this the full story? In Ref. [107], Payne *et al.* revisited the evidence of spin precession in GW200129 [108]. They concluded that the evidence for spin precession originates from the LIGO Livingston data, in the 20–50 Hz frequency range, alone. This range coincides with the frequency range that displays data quality issues, due to a glitch in the detector that overlapped in time with the signal [19]. By reanalyzing the GW200129 data with $f_{\rm low} > 50$ Hz (while leaving LIGO Hanford data intact and not using Virgo data), they showed that the evidence in favor of spin precession in this event disappears. See Ref. [107] for a detailed discussion. Moreover, a reanalysis of the LIGO Livingston glitch mitigation showed that the difference between the spin-precessing and nonprecessing interpretations of this event is subdominant relative to uncertainties in the glitch subtraction [107]. Since we have used the glitch-subtracted data in our parameter estimation, we are then led to the second conclusion of our study of this event, namely that, issues with data quality can introduce biases in non-GR parameters, to an extent that one can find significant false violations of GR in GW events detected with present GW observatories. See Ref. [109] for a recent study of this issue.

Furthermore, we repeat here the analysis we have performed for GW150914 where we considered $\boldsymbol{\vartheta}_{\rm nGR} = \{\delta A, \delta f_{220}, \delta\tau_{220}\}$ as our non-GR parameters. For the discussion that follows, we assume that GW200129 is an unmistakable genuine spin-precessing BBH. We show our results in Fig. 14. We see that while our inferred values of δf_{220} and $\delta\tau_{220}$ are consistent with GR at 90% confidence level, our inference of the amplitude parameter, $\delta A = 0.50^{+0.46}_{-0.30}$ at 90% credible level, remains inconsistent with GR. Moreover, this value hardly changes from our $\{\delta A, \delta\omega\}$-study, i.e., $\delta A = 0.44^{+0.38}_{-0.28}$, at the same credible level.

This result is interesting for two reasons. First, it indicates that the systematic error caused by spin-precession mismodeling is robust to the inclusion of deformations to the ringdown QNM frequencies, at least for this event. Second, there is a commonality between our finding for GW150914 (see Fig. 12) and GW200129 (see Fig. 14) namely, that in both cases the posterior distributions of δf_{220} and $\delta\tau_{220}$ are consistent with GR, despite the larger parameter space due to the inclusion of δA. In the case in which one considers only δf_{220} and $\delta\tau_{220}$ as non-GR parameter, the consistency with GR had already been established in Ref. [40], and in particular in Ref. [13]; see Sec. VIII, Fig. 14 there.[2] Our analysis of these two GW

[2]The LVK Collaboration also does an independent analysis of the ringdown using pyRing. This analysis lead to an odds ratio $\log_{10}\mathcal{O}^{\rm nGR}_{\rm GR} = -0.09$ for GW200129, the largest among all events studied [11]. A positive value would quantify the level of disagreement with GR.

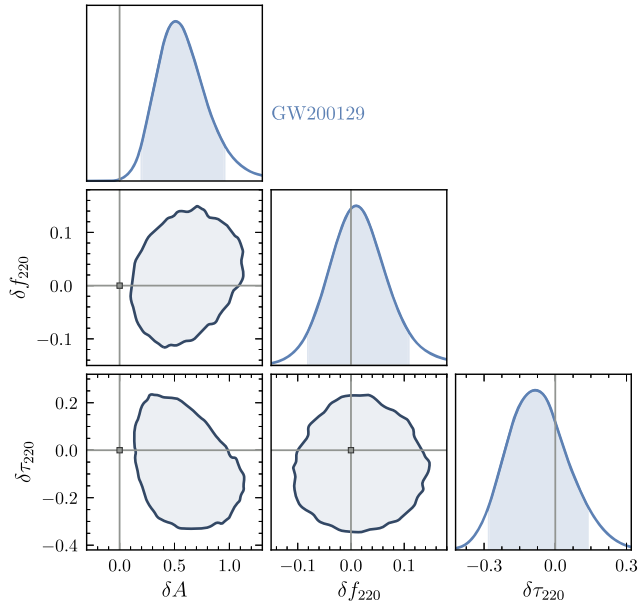

FIG. 14. The one- and two-dimensional posterior distribution functions for δA, δf_{220}, and $\delta\tau_{220}$ for GW200129. All contours indicate 90% credible regions. We see that while our inferred values for δf_{220} and $\delta\tau_{220}$ are consistent with GR, δA is not.

events with the new pSEOBNRHM waveform model suggests the following: the model would be able to detect deviations from nonprecessing quasicircular GW signals in the plunge-merger ringdown which otherwise would not be seen when having deformations to the ringdown only.

We close our discussion of GW200129 with two remarks. First, data-quality issues aside, we can think of our spin-precessing injection studies as illustrative of what could happen in upcoming LVK observation runs. By doing so, we have then demonstrated the existence of a systematic error on the non-GR parameters caused by spin-precession mismodeling.[3] Second, although we have proposed pSEOBNRHM as a means of constraining (or detecting) potential non-GR physics in BBH coalescences, we can also interpret the merger parameters as indicators of our ignorance in GR waveform modeling.[4] More concretely, in a hypothetical scenario where GW modelers did not know that BBH can spin precess, an analysis of GW200129 with pSEOBNRHM would suggest that their model of the peak GW-mode amplitudes is insufficient to describe this event and hence be an indicative of new, nonmodeled binary dynamics that was absent in their waveform model. They would not be able to say that spin precession is the missing dynamics, but they would at least realize that something is missing.

VIII. DISCUSSIONS AND FINAL REMARKS

We presented a time-domain IMR waveform model that accommodates parametrized deviations from GR in the plunge-merger-ringdown stage of nonprecessing and quasicircular BBHs. This model generalizes the previous iterations of the pSEOBNRHM model [38–40], which included deviations from GR in the inspiral phase or modified the QNM frequencies only, by introducing deformations parameters $\boldsymbol{\vartheta}^{\rm merger}_{\rm nGR}$ that, for each GW mode, can change the time at which the GW mode peaks, the mode frequency at this instant, and the peak mode amplitude. This new version of pSEOBNRHM reduces to the state-of-the-art SEOBNRHM model [63,64,71] for nonprecessing and quasicircular BBHs in the limit in which all deformations parameters are set to zero.

We used pSEOBNRHM to perform a series of injections studies for GW150914-like events exploring (i) the constraints that one could place on these non-GR parameters, (ii) the biases introduced on the intrinsic binary parameters in case nature is not described by GR and we model the signal with a GR template, and, finally, and (iii) we studied the measurability of these non-GR parameters.

We also used pSEOBNRHM in a reanalysis of GW150914 and GW200129. For GW150914, we found that the deviations from the GR peak amplitude and the instantaneous GW frequency can already be constrained to about 20% at 90% credible level. For GW200129, we found an interesting interplay between spin precession and false violations of GR that manifests as a $\sim 2\sigma$ deviation from GR in the peak amplitude parameter. By interpreting the evidence for spin precession in this event as due to data-quality issues in the LIGO Livingston detector [19,107], we found a further a connection between data-quality issues and false violations of GR [109].

These results warrant further studies on the systematic bias due to spin precession in tests of GR. In the context of plunge-merger-ringdown test, this could be achieved by extending the SEOBNRv4PHM waveform model [65] to include the same set of non-GR parameters $\boldsymbol{\vartheta}_{\rm nGR}$ used here. It is also natural to explore which systematic effects higher GW modes [110] and binary eccentricity can introduce in tests of GR. For the latter, see Ref. [111] for work in this direction for IMR consistency tests [60,112] and Ref. [113] in the context of deviations in the post-Newtonian (PN) GW phasing [31,36,114]. It would also be interesting to investigate these issues in the context of the ringdown test within the EOB framework employed by LVK Collaboration [13] and which relies on pSEOBNRHM [39,40]. This could be done by adding non-GR deformations to the SEOBNRv4EHM waveform model of Ref. [115]. It would also be important to investigate whether pSEOBNRHM can

[3]If the GW signal had a smaller total-mass binary, signatures of spin precession could have been observed from the inspiral portion of the waveform only.

[4]In this interpretation, the questions we investigated in Secs. V A and V B become: (i) how large are the systematic errors in one's parameter inference due to GW modeling? and (ii) how large can our GW-modeling uncertainties be such that we are still consistent with the "true" binary parameters?

be used to detect signatures of non-GR physics, as predicted by the rapidly growing field of NR in modified gravity theories (see e.g., Refs. [116–125]); some of which predict nonperturbative departures from GR only in late-inspiral and merger ringdown [126–129]. One could also study what the theory-agnostic bounds we obtained with GW150914 on the amplitude and GW frequency imply to the free parameters of various modified gravity theories.

The deformations parameters $\vartheta_{\rm nGR}^{\rm merger}$ in our pSEOBNRHM model should have an approximate correspondence to the phenomenological deviation parameters (from NR calibrated values) in the "intermediate region" of the IMRPhenom waveform model used in the TIGER pipeline [35–37] of the LVK Collaboration [9–12]. Such a mapping could be derived through synthetic injection studies. This work only introduced non-GR parameters in the EOB GW modes and only during the plunge-merger-ringdown. Importantly, and more consistently, in the near future we will extend the parametrization to the EOB conservative and dissipative dynamics.

The interplay between GW waveform systematics, characterization and subtraction of nontransient Gaussian noises in GW detectors, and non-GR physics will become increasingly important in the future. Planned ground-based [130,131] and space-borne GW observatories [132] will detect GW transients with SNRs that may reach the thousands depending on the source. Having all these aspects under control is a daunting task that will need to be faced if one wants to confidently answer the question "Is Einstein still right?" [133] in the stage of BBH coalescences where his theory unveils its most outlandish aspects.

ACKNOWLEDGMENTS

We thank Héctor Estellés, Ajit Kumar Mehta, Deyan Mihaylov, Serguei Ossokine, Harald Pfeiffer, Lorenzo Pompili, Antoni Ramos-Buades, and Helvi Witek for discussions. We also thank Nathan Johnson-McDaniel, Juan Calderón Bustillo, and Gregorio Carullo for comments on this work. We acknowledge funding from the Deutsche Forschungsgemeinschaft (DFG) Project No. 386119226. We also acknowledge the computational resources provided by the Max Planck Institute for Gravitational Physics (Albert Einstein Institute), Potsdam, in particular, the Hypatia cluster. The material presented in this paper is based upon work supported by National Science Foundation's (NSF) LIGO Laboratory, which is a major facility fully funded by the NSF. This research has made use of data or software obtained from the Gravitational Wave Open Science Center ([134]), a service of LIGO Laboratory, the LIGO Scientific Collaboration, the Virgo Collaboration, and KAGRA. LIGO Laboratory and Advanced LIGO are funded by the United States National Science Foundation (NSF) as well as the Science and Technology Facilities Council (STFC) of the United Kingdom, the Max-Planck-Society (MPS), and the State of Niedersachsen/Germany for support of the construction of Advanced LIGO and construction and operation of the GEO600 detector. Additional support for Advanced LIGO was provided by the Australian Research Council. Virgo is funded, through the European Gravitational Observatory (EGO), by the French Centre National de Recherche Scientifique (CNRS), the Italian Istituto Nazionale di Fisica Nucleare (INFN) and the Dutch Nikhef, with contributions by institutions from Belgium, Germany, Greece, Hungary, Ireland, Japan, Monaco, Poland, Portugal, Spain. KAGRA is supported by Ministry of Education, Culture, Sports, Science and Technology (MEXT), Japan Society for the Promotion of Science (JSPS) in Japan; National Research Foundation (NRF) and Ministry of Science and ICT (MSIT) in Korea; Academia Sinica (AS) and National Science and Technology Council (NSTC) in Taiwan [97].

APPENDIX: ESTIMATION OF THE INTRINSIC BINARY PARAMETERS

In this appendix, we compare the posterior distributions on the intrinsic binary parameters obtained using the SEOBNRHM and pSEOBNRHM waveform models. This complements the results shown in Sec. V B (Fig. 15) and Sec. VI (Fig. 16). For simplicity, we focus on the total mass M, the mass ratio q, the effective spin $\chi_{\rm eff}$ and the luminosity distance $D_{\rm L}$.

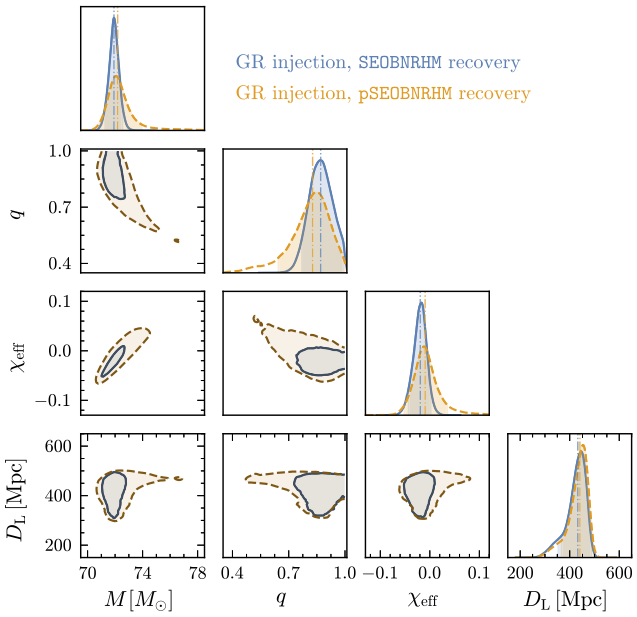

FIG. 15. The one- and two-dimensional posterior distributions on the intrinsic binary parameters of the total mas M, the mass ratio q, the effective spin $\chi_{\rm eff}$, and the luminosity distance $D_{\rm L}$ for a GR injection with the parameters in Table II. The parameter estimation is performed using SEOBNRHM (solid curves) and pSEOBNRHM (dashed curves) waveform models. All contours indicate 90% credible regions and the vertical lines mark the inferred median values for each parameter.

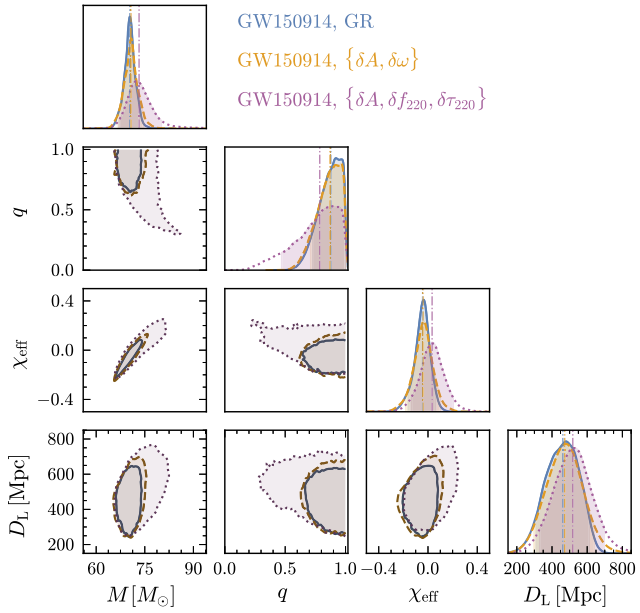

FIG. 16. The one- and two-dimensional posterior distributions on the intrinsic binary parameters of the total mass M, the mass ratio q, the effective spin $\chi_{\rm eff}$ and the luminosity distance $D_{\rm L}$ for GW150914. The parameter estimation is done with SEOBNRHM (solid curves) and pSEOBNRHM waveform model with non-GR parameters $\{\delta A, \delta\omega\}$ (dashed curves) and $\{\delta A, \delta f_{220}, \delta\tau_{220}\}$ (dotted curves). All contours indicate 90% credible regions and the vertical lines mark the inferred median values for each parameter.

Figure 15 shows the posterior distributions on the intrinsic binary parameters for a GR signal with the properties shown in Table II. The solid curves are obtained when the parameter estimation is performed with the GR waveform model SEOBNRHM, whereas the dashed curves are obtained with the parametrized plunge-merger-ringdown waveform model pSEOBNRHM (cf. Sec. V B). In both cases, the SNR is 98. We see that the 90% confidence intervals of the posterior distributions in the two analyses overlap in the parameter space. The most important difference is that the 90% credible intervals are wider in the pSEOBNRHM analysis. There are also changes to the median values of the binary parameters, as can be seen through the vertical lines in the plot.

To be more precise, the posteriors of the pSEOBNRHM model have a tail, most evidently in the mass ratio q. For the mass ratio, at 90% confidence interval, we find $q = 0.87^{+0.12}_{-0.10}$ (for the SEOBNRHM recovery) and $q = 0.84^{+0.15}_{-0.20}$ (for the pSEOBNRHM recovery). The broader posteriors, and tails, are due to the fact that the pSEOBNRHM model has five additional parameters with respect to SEOBNRHM. Qualitatively, by increasing the number of parameters in the model we increase the number of possible waveforms that match, to some extent, the injected signal. This will be most evidently seen in Fig. 16 which we discuss below.

Figure 16 shows the posterior distributions on the intrinsic binary parameters for our analyses of GW150914 (cf. Sec. VI). The solid curves are obtained when we use SEOBNRHM for parameter estimation, whereas the dashed and dotted curves are obtained when we use pSEOBNRHM with non-GR parameters $\{\delta A, \delta\omega\}$ ("merger test of GR") and $\{\delta A, \delta f_{220}, \delta\tau_{220}\}$ ("merger-ringdown test of GR"), respectively. The figure is similar to Fig. 15, discussed above. Again, we see that the 90% confidence intervals of the posterior distributions in the three analyses overlap in the parameter space. However, here we can see more explicitly how the increase of extra non-GR parameters in the waveform model results in wider posteriors and tails appearance.

[1] C. M. Will, The confrontation between general relativity and experiment, Living Rev. Relativity **17**, 4 (2014).
[2] T. Clifton, P. G. Ferreira, A. Padilla, and C. Skordis, Modified gravity and cosmology, Phys. Rep. **513**, 1 (2012).
[3] D. J. Kapner, T. S. Cook, E. G. Adelberger, J. H. Gundlach, B. R. Heckel, C. D. Hoyle, and H. E. Swanson, Tests of the Gravitational Inverse-Square Law Below the Dark-Energy Length Scale, Phys. Rev. Lett. **98**, 021101 (2007).
[4] J. G. Lee, E. G. Adelberger, T. S. Cook, S. M. Fleischer, and B. R. Heckel, New Test of the Gravitational $1/r^2$ Law at Separations Down to 52 μm, Phys. Rev. Lett. **124**, 101101 (2020).
[5] R. Abuter *et al.* (GRAVITY Collaboration), Detection of the Schwarzschild precession in the orbit of the star S2 near the Galactic centre massive black hole, Astron. Astrophys. **636**, L5 (2020).
[6] M. Kramer *et al.*, Strong-Field Gravity Tests with the Double Pulsar, Phys. Rev. X **11**, 041050 (2021).
[7] K. Akiyama *et al.* (Event Horizon Telescope Collaboration), First M87 Event Horizon Telescope results. V. Physical origin of the asymmetric ring, Astrophys. J. Lett. **875**, L5 (2019).
[8] K. Akiyama *et al.* (Event Horizon Telescope Collaboration), First Sagittarius A* Event Horizon Telescope results. VI. Testing the black hole metric, Astrophys. J. Lett. **930**, L17 (2022).
[9] B. P. Abbott *et al.* (LIGO Scientific and Virgo Collaborations), Tests of General Relativity with GW150914, Phys. Rev. Lett. **116**, 221101 (2016); **121**, 129902(E) (2018).

[10] B. P. Abbott *et al.* (LIGO Scientific and Virgo Collaborations), Tests of General Relativity with GW170817, Phys. Rev. Lett. **123**, 011102 (2019).
[11] B. P. Abbott *et al.* (LIGO Scientific and Virgo Collaborations), Tests of general relativity with the binary black hole signals from the LIGO-Virgo catalog GWTC-1, Phys. Rev. D **100**, 104036 (2019).
[12] R. Abbott *et al.* (LIGO Scientific and Virgo Collaborations), Tests of general relativity with binary black holes from the second LIGO-Virgo gravitational-wave transient catalog, Phys. Rev. D **103**, 122002 (2021).
[13] R. Abbott *et al.* (LIGO Scientific, Virgo, and KAGRA Collaborations), Tests of general relativity with GWTC-3, arXiv:2112.06861.
[14] B. P. Abbott *et al.* (LIGO Scientific and Virgo Collaborations), Observation of Gravitational Waves from a Binary Black Hole Merger, Phys. Rev. Lett. **116**, 061102 (2016).
[15] B. P. Abbott *et al.* (LIGO Scientific and Virgo Collaborations), Properties of the Binary Black Hole Merger GW150914, Phys. Rev. Lett. **116**, 241102 (2016).
[16] B. P. Abbott *et al.* (LIGO Scientific and Virgo Collaborations), GWTC-1: A Gravitational-Wave Transient Catalog of Compact Binary Mergers Observed by LIGO and Virgo during the First and Second Observing Runs, Phys. Rev. X **9**, 031040 (2019).
[17] R. Abbott *et al.* (LIGO Scientific and Virgo Collaborations), GWTC-2: Compact Binary Coalescences Observed by LIGO and Virgo During the First Half of the Third Observing Run, Phys. Rev. X **11**, 021053 (2021).
[18] R. Abbott *et al.* (LIGO Scientific and Virgo Collaborations), GWTC-2.1: Deep extended catalog of compact binary coalescences observed by LIGO and Virgo during the first half of the third observing run, arXiv:2108.01045 [Phys. Rev. D (to be published)].
[19] R. Abbott *et al.* (LIGO Scientific, Virgo, KAGRA Collaborations), GWTC-3: Compact Binary Coalescences Observed by LIGO and Virgo During the Second Part of the Third Observing Run, arXiv:2111.03606 [Phys. Rev. X (to be published)].
[20] R. Abbott *et al.* (LIGO Scientific, KAGRA, Virgo Collaborations), Observation of gravitational waves from two neutron star–black hole coalescences, Astrophys. J. Lett. **915**, L5 (2021).
[21] B. P. Abbott *et al.* (LIGO Scientific and Virgo Collaborations), GW170817: Observation of Gravitational Waves from a Binary Neutron Star Inspiral, Phys. Rev. Lett. **119**, 161101 (2017).
[22] B. P. Abbott *et al.* (LIGO Scientific and Virgo Collaborations), GW190425: Observation of a compact binary coalescence with total mass $\sim 3.4 M_{\odot}$, Astrophys. J. Lett. **892**, L3 (2020).
[23] J. Aasi *et al.* (LIGO Scientific Collaboration), Advanced LIGO, Classical Quantum Gravity **32**, 074001 (2015).
[24] F. Acernese *et al.* (Virgo Collaboration), Advanced Virgo: A second-generation interferometric gravitational wave detector, Classical Quantum Gravity **32**, 024001 (2015).
[25] M. Saleem, S. Datta, K. G. Arun, and B. S. Sathyaprakash, Parametrized tests of post-Newtonian theory using principal component analysis, Phys. Rev. D **105**, 084062 (2022).
[26] L. Blanchet and B. S. Sathyaprakash, Detecting the Tail Effect in Gravitational Wave Experiments, Phys. Rev. Lett. **74**, 1067 (1995).
[27] K. G. Arun, B. R. Iyer, M. S. S. Qusailah, and B. S. Sathyaprakash, Testing post-Newtonian theory with gravitational wave observations, Classical Quantum Gravity **23**, L37 (2006).
[28] K. G. Arun, B. R. Iyer, M. S. S. Qusailah, and B. S. Sathyaprakash, Probing the non-linear structure of general relativity with black hole binaries, Phys. Rev. D **74**, 024006 (2006).
[29] Y. Pan, A. Buonanno, J. G. Baker, J. Centrella, B. J. Kelly, S. T. McWilliams, F. Pretorius, and J. R. van Meter, A data-analysis driven comparison of analytic and numerical coalescing binary waveforms: Nonspinning case, Phys. Rev. D **77**, 024014 (2008).
[30] P. Ajith *et al.*, A Template bank for gravitational waveforms from coalescing binary black holes. I. Non-spinning binaries, Phys. Rev. D **77**, 104017 (2008); **79**, 129901(E) (2009).
[31] N. Yunes and F. Pretorius, Fundamental theoretical bias in gravitational wave astrophysics and the parameterized post-Einsteinian framework, Phys. Rev. D **80**, 122003 (2009).
[32] L. Sampson, N. Cornish, and N. Yunes, Mismodeling in gravitational-wave astronomy: The trouble with templates, Phys. Rev. D **89**, 064037 (2014).
[33] S. Gossan, J. Veitch, and B. S. Sathyaprakash, Bayesian model selection for testing the no-hair theorem with black hole ringdowns, Phys. Rev. D **85**, 124056 (2012).
[34] J. Meidam, M. Agathos, C. Van Den Broeck, J. Veitch, and B. S. Sathyaprakash, Testing the no-hair theorem with black hole ringdowns using TIGER, Phys. Rev. D **90**, 064009 (2014).
[35] T. G. F. Li, W. Del Pozzo, S. Vitale, C. Van Den Broeck, M. Agathos, J. Veitch, K. Grover, T. Sidery, R. Sturani, and A. Vecchio, Towards a generic test of the strong field dynamics of general relativity using compact binary coalescence, Phys. Rev. D **85**, 082003 (2012).
[36] M. Agathos, W. Del Pozzo, T. G. F. Li, C. Van Den Broeck, J. Veitch, and S. Vitale, TIGER: A data analysis pipeline for testing the strong-field dynamics of general relativity with gravitational wave signals from coalescing compact binaries, Phys. Rev. D **89**, 082001 (2014).
[37] J. Meidam *et al.*, Parametrized tests of the strong-field dynamics of general relativity using gravitational wave signals from coalescing binary black holes: Fast likelihood calculations and sensitivity of the method, Phys. Rev. D **97**, 044033 (2018).
[38] A. K. Mehta, A. Buonanno, R. Cotesta, A. Ghosh, N. Sennett, and J. Steinhoff, Tests of general relativity with gravitational-wave observations using a flexible-theory-independent method, Phys. Rev. D **107**, 044020 (2023).
[39] R. Brito, A. Buonanno, and V. Raymond, Black-hole spectroscopy by making full use of gravitational-wave modeling, Phys. Rev. D **98**, 084038 (2018).
[40] A. Ghosh, R. Brito, and A. Buonanno, Constraints on quasinormal-mode frequencies with LIGO-Virgo binary–black-hole observations, Phys. Rev. D **103**, 124041 (2021).

[41] G. Carullo *et al.*, Empirical tests of the black hole no-hair conjecture using gravitational-wave observations, Phys. Rev. D **98**, 104020 (2018).
[42] G. Carullo, W. Del Pozzo, and J. Veitch, Observational black hole spectroscopy: A time-domain multimode analysis of GW150914, Phys. Rev. D **99**, 123029 (2019); **100**, 089903(E) (2019).
[43] M. Isi, M. Giesler, W. M. Farr, M. A. Scheel, and S. A. Teukolsky, Testing the No-Hair Theorem with GW150914, Phys. Rev. Lett. **123**, 111102 (2019).
[44] G. Carullo, G. Riemenschneider, K. W. Tsang, A. Nagar, and W. Del Pozzo, GW150914 peak frequency: A novel consistency test of strong-field general relativity, Classical Quantum Gravity **36**, 105009 (2019).
[45] M. Isi, K. Chatziioannou, and W. M. Farr, Hierarchical Test of General Relativity with Gravitational Waves, Phys. Rev. Lett. **123**, 121101 (2019).
[46] K. W. Tsang, A. Ghosh, A. Samajdar, K. Chatziioannou, S. Mastrogiovanni, M. Agathos, and C. Van Den Broeck, A morphology-independent search for gravitational wave echoes in data from the first and second observing runs of Advanced LIGO and Advanced Virgo, Phys. Rev. D **101**, 064012 (2020).
[47] S. Bhagwat and C. Pacilio, Merger-ringdown consistency: A new test of strong gravity using deep learning, Phys. Rev. D **104**, 024030 (2021).
[48] M. Okounkova, W. M. Farr, M. Isi, and L. C. Stein, Constraining gravitational wave amplitude birefringence and Chern-Simons gravity with GWTC-2, Phys. Rev. D **106**, 044067 (2022).
[49] Y.-F. Wang, S. M. Brown, L. Shao, and W. Zhao, Tests of gravitational-wave birefringence with the open gravitational-wave catalog, Phys. Rev. D **106**, 084005 (2022).
[50] M. Saleem, N. V. Krishnendu, A. Ghosh, A. Gupta, W. Del Pozzo, A. Ghosh, and K. G. Arun, Population inference of spin-induced quadrupole moments as a probe for nonblack hole compact binaries, Phys. Rev. D **105**, 104066 (2022).
[51] L. Haegel, K. O'Neal-Ault, Q. G. Bailey, J. D. Tasson, M. Bloom, and L. Shao, Search for anisotropic, birefringent spacetime-symmetry breaking in gravitational wave propagation from GWTC-3, Phys. Rev. D **107**, 064031 (2023).
[52] A. Buonanno and T. Damour, Effective one-body approach to general relativistic two-body dynamics, Phys. Rev. D **59**, 084006 (1999).
[53] A. Buonanno and T. Damour, Transition from inspiral to plunge in binary black hole coalescences, Phys. Rev. D **62**, 064015 (2000).
[54] T. Damour, P. Jaranowski, and G. Schaefer, On the determination of the last stable orbit for circular general relativistic binaries at the third postNewtonian approximation, Phys. Rev. D **62**, 084011 (2000).
[55] T. Damour, Coalescence of two spinning black holes: An effective one-body approach, Phys. Rev. D **64**, 124013 (2001).
[56] A. Buonanno, Y. Chen, and T. Damour, Transition from inspiral to plunge in precessing binaries of spinning black holes, Phys. Rev. D **74**, 104005 (2006).
[57] E. Barausse and A. Buonanno, An Improved effective-one-body Hamiltonian for spinning black-hole binaries, Phys. Rev. D **81**, 084024 (2010).
[58] T. Damour, B. R. Iyer, and A. Nagar, Improved resummation of post-Newtonian multipolar waveforms from circularized compact binaries, Phys. Rev. D **79**, 064004 (2009).
[59] Y. Pan, A. Buonanno, R. Fujita, E. Racine, and H. Tagoshi, Post-Newtonian factorized multipolar waveforms for spinning, non-precessing black-hole binaries, Phys. Rev. D **83**, 064003 (2011); **87**, 109901(E) (2013).
[60] A. Ghosh *et al.*, Testing general relativity using golden black-hole binaries, Phys. Rev. D **94**, 021101 (2016).
[61] A. Ghosh, N. K. Johnson-Mcdaniel, A. Ghosh, C. K. Mishra, P. Ajith, W. Del Pozzo, C. P. L. Berry, A. B. Nielsen, and L. London, Testing general relativity using gravitational wave signals from the inspiral, merger and ringdown of binary black holes, Classical Quantum Gravity **35**, 014002 (2018).
[62] N. K. Johnson-McDaniel, A. Ghosh, S. Ghonge, M. Saleem, N. V. Krishnendu, and J. A. Clark, Investigating the relation between gravitational wave tests of general relativity, Phys. Rev. D **105**, 044020 (2022).
[63] A. Bohé *et al.*, Improved effective-one-body model of spinning, nonprecessing binary black holes for the era of gravitational-wave astrophysics with advanced detectors, Phys. Rev. D **95**, 044028 (2017).
[64] R. Cotesta, A. Buonanno, A. Bohé, A. Taracchini, I. Hinder, and S. Ossokine, Enriching the symphony of gravitational waves from binary black holes by tuning higher harmonics, Phys. Rev. D **98**, 084028 (2018).
[65] S. Ossokine *et al.*, Multipolar effective-one-body waveforms for precessing binary black holes: Construction and validation, Phys. Rev. D **102**, 044055 (2020).
[66] A. Nagar *et al.*, Time-domain effective-one-body gravitational waveforms for coalescing compact binaries with nonprecessing spins, tides and self-spin effects, Phys. Rev. D **98**, 104052 (2018).
[67] A. Nagar, G. Riemenschneider, G. Pratten, P. Rettegno, and F. Messina, Multipolar effective one body waveform model for spin-aligned black hole binaries, Phys. Rev. D **102**, 024077 (2020).
[68] R. Gamba, S. Akçay, S. Bernuzzi, and J. Williams, Effective-one-body waveforms for precessing coalescing compact binaries with post-Newtonian twist, Phys. Rev. D **106**, 024020 (2022).
[69] E. T. Newman and R. Penrose, Note on the Bondi-Metzner-Sachs group, J. Math. Phys. (N.Y.) **7**, 863 (1966).
[70] H. O. Silva, A. Ghosh, and A. Buonanno, Black-hole ringdown as a probe of higher-curvature gravity theories, Phys. Rev. D **107**, 044030 (2023).
[71] D. P. Mihaylov, S. Ossokine, A. Buonanno, and A. Ghosh, Fast post-adiabatic waveforms in the time domain: Applications to compact binary coalescences in LIGO and Virgo, Phys. Rev. D **104**, 124087 (2021).
[72] A. Buonanno, Y. Pan, J. G. Baker, J. Centrella, B. J. Kelly, S. T. McWilliams, and J. R. van Meter, Toward faithful templates for non-spinning binary black holes using the effective-one-body approach, Phys. Rev. D **76**, 104049 (2007).
[73] J. Abadie *et al.* (LIGO Scientific and Virgo Collaborations), Search for gravitational waves from binary black hole inspiral, merger and ringdown, Phys. Rev. D **83**, 122005 (2011); **86**, 069903(E) (2012).

[74] T. Damour, A. Nagar, and S. Bernuzzi, Improved effective-one-body description of coalescing nonspinning black-hole binaries and its numerical-relativity completion, Phys. Rev. D **87**, 084035 (2013).
[75] A. Nagar and P. Rettegno, Efficient effective one body time-domain gravitational waveforms, Phys. Rev. D **99**, 021501 (2019).
[76] P. Rettegno, F. Martinetti, A. Nagar, D. Bini, G. Riemenschneider, and T. Damour, Comparing effective one body Hamiltonians for spin-aligned coalescing binaries, Phys. Rev. D **101**, 104027 (2020).
[77] A. Taracchini, Y. Pan, A. Buonanno, E. Barausse, M. Boyle, T. Chu, G. Lovelace, H. P. Pfeiffer, and M. A. Scheel, Prototype effective-one-body model for nonprecessing spinning inspiral-merger-ringdown waveforms, Phys. Rev. D **86**, 024011 (2012).
[78] T. Damour and A. Nagar, Faithful effective-one-body waveforms of small-mass-ratio coalescing black-hole binaries, Phys. Rev. D **76**, 064028 (2007).
[79] E. Barausse, A. Buonanno, S. A. Hughes, G. Khanna, S. O'Sullivan, and Y. Pan, Modeling multipolar gravitational-wave emission from small mass-ratio mergers, Phys. Rev. D **85**, 024046 (2012).
[80] A. Taracchini, A. Buonanno, G. Khanna, and S. A. Hughes, Small mass plunging into a Kerr black hole: Anatomy of the inspiral-merger-ringdown waveforms, Phys. Rev. D **90**, 084025 (2014).
[81] R. H. Price and G. Khanna, Arrival times of gravitational radiation peaks for binary inspiral, Phys. Rev. D **94**, 104026 (2016).
[82] C. V. Vishveshwara, Scattering of gravitational radiation by a Schwarzschild black-hole, Nature (London) **227**, 936 (1970).
[83] W. H. Press, Long wave trains of gravitational waves from a vibrating black hole, Astrophys. J. Lett. **170**, L105 (1971).
[84] S. L. Detweiler, Black holes and gravitational waves. III. The resonant frequencies of rotating holes, Astrophys. J. **239**, 292 (1980).
[85] M. Boyle *et al.*, The SXS Collaboration catalog of binary black hole simulations, Classical Quantum Gravity **36**, 195006 (2019).
[86] M. Boyle, A. Buonanno, L. E. Kidder, A. H. Mroué, Y. Pan, H. P. Pfeiffer, and M. A. Scheel, High-accuracy numerical simulation of black-hole binaries: Computation of the gravitational-wave energy flux and comparisons with post-Newtonian approximants, Phys. Rev. D **78**, 104020 (2008).
[87] A. Taracchini *et al.*, Effective-one-body model for black-hole binaries with generic mass ratios and spins, Phys. Rev. D **89**, 061502 (2014).
[88] M. Isi and W. M. Farr, Analyzing black-hole ringdowns, arXiv:2107.05609.
[89] A. Buonanno, Y. Pan, H. P. Pfeiffer, M. A. Scheel, L. T. Buchman, and L. E. Kidder, Effective-one-body waveforms calibrated to numerical relativity simulations: Coalescence of non-spinning, equal-mass black holes, Phys. Rev. D **79**, 124028 (2009).
[90] Y. Pan, A. Buonanno, M. Boyle, L. T. Buchman, L. E. Kidder, H. P. Pfeiffer, and M. A. Scheel, Inspiral-merger-ringdown multipolar waveforms of nonspinning black-hole binaries using the effective-one-body formalism, Phys. Rev. D **84**, 124052 (2011).
[91] C. Rover, R. Meyer, and N. Christensen, Bayesian inference on compact binary inspiral gravitational radiation signals in interferometric data, Classical Quantum Gravity **23**, 4895 (2006).
[92] M. van der Sluys, V. Raymond, I. Mandel, C. Rover, N. Christensen, V. Kalogera, R. Meyer, and A. Vecchio, Parameter estimation of spinning binary inspirals using Markov-chain Monte Carlo, Classical Quantum Gravity **25**, 184011 (2008).
[93] J. Veitch *et al.*, Parameter estimation for compact binaries with ground-based gravitational-wave observations using the LALInference software library, Phys. Rev. D **91**, 042003 (2015).
[94] LIGO Scientific Collaboration, LIGO Algorithm Library—LALSuite, free software (GPL) (2018), https://git.ligo.org/lscsoft/lalsuite.
[95] L. Barsotti, P. Fritschel, M. Evans, and S. Gras, Updated Advanced LIGO sensitivity design curve, Technical Report, 2018, https://dcc.ligo.org/LIGO-T1800044/public.
[96] M. Vallisneri and N. Yunes, Stealth bias in gravitational-wave parameter estimation, Phys. Rev. D **87**, 102002 (2013).
[97] R. Abbott *et al.* (LIGO Scientific and Virgo Collaborations), Open data from the first and second observing runs of Advanced LIGO and Advanced Virgo, SoftwareX **13**, 100658 (2021).
[98] LIGO Scientific, Virgo, and KAGRA Collaborations, GWTC-3: Compact binary coalescences observed by LIGO and Virgo during the second part of the third observing run—parameter estimation data release (2021), https://zenodo.org/record/5546663.
[99] G. Pratten *et al.*, Computationally efficient models for the dominant and subdominant harmonic modes of precessing binary black holes, Phys. Rev. D **103**, 104056 (2021).
[100] C. Pankow, P. Brady, E. Ochsner, and R. O'Shaughnessy, Novel scheme for rapid parallel parameter estimation of gravitational waves from compact binary coalescences, Phys. Rev. D **92**, 023002 (2015).
[101] J. Lange *et al.*, Parameter estimation method that directly compares gravitational wave observations to numerical relativity, Phys. Rev. D **96**, 104041 (2017).
[102] D. Wysocki, R. O'Shaughnessy, J. Lange, and Y.-L. L. Fang, Accelerating parameter inference with graphics processing units, Phys. Rev. D **99**, 084026 (2019).
[103] G. Ashton *et al.*, Bilby: A user-friendly Bayesian inference library for gravitational-wave astronomy, Astrophys. J. Suppl. Ser. **241**, 27 (2019).
[104] I. M. Romero-Shaw *et al.*, Bayesian inference for compact binary coalescences with Bilby: Validation and application to the first LIGO–Virgo gravitational-wave transient catalogue, Mon. Not. R. Astron. Soc. **499**, 3295 (2020).
[105] V. Varma, S. E. Field, M. A. Scheel, J. Blackman, D. Gerosa, L. C. Stein, L. E. Kidder, and H. P. Pfeiffer, Surrogate models for precessing binary black hole simulations with unequal masses, Phys. Rev. Res. **1**, 033015 (2019).

[106] S. E. Field, C. R. Galley, J. S. Hesthaven, J. Kaye, M. Tiglio, J. Blackman, B. Szilágyi, M. A. Scheel, D. A. Hemberger, P. Schmidt, R. Smith, C. D. Ott, M. Boyle, L. E. Kidder, H. P. Pfeiffer, and V. Varma, Binary black-hole surrogate waveform catalog (2022), https://zenodo.org/record/6726994.

[107] E. Payne, S. Hourihane, J. Golomb, R. Udall, R. Udall, D. Davis, and K. Chatziioannou, Curious case of GW200129: Interplay between spin-precession inference and data-quality issues, Phys. Rev. D **106**, 104017 (2022).

[108] M. Hannam, C. Hoy, J. E. Thompson, S. Fairhurst, V. Raymond *et al.*, General-relativistic precession in a black-hole binary, Nature (London) **610**, 652 (2022).

[109] J. Y. L. Kwok, R. K. L. Lo, A. J. Weinstein, and T. G. F. Li, Investigation of the effects of non-Gaussian noise transients and their mitigation in parameterized gravitational-wave tests of general relativity, Phys. Rev. D **105**, 024066 (2022).

[110] P. T. H. Pang, J. Calderón Bustillo, Y. Wang, and T. G. F. Li, Potential observations of false deviations from general relativity in gravitational wave signals from binary black holes, Phys. Rev. D **98**, 024019 (2018).

[111] S. A. Bhat, P. Saini, M. Favata, and K. G. Arun, Systematic bias on the inspiral-merger-ringdown consistency test due to neglect of orbital eccentricity, Phys. Rev. D **107**, 024009 (2023).

[112] S. A. Hughes and K. Menou, Golden binaries for LISA: Robust probes of strong-field gravity, Astrophys. J. **623**, 689 (2005).

[113] P. Saini, M. Favata, and K. G. Arun, Systematic bias on parametrized tests of general relativity due to neglect of orbital eccentricity, Phys. Rev. D **106**, 084031 (2022).

[114] N. Cornish, L. Sampson, N. Yunes, and F. Pretorius, Gravitational wave tests of general relativity with the parameterized post-Einsteinian framework, Phys. Rev. D **84**, 062003 (2011).

[115] A. Ramos-Buades, A. Buonanno, M. Khalil, and S. Ossokine, Effective-one-body multipolar waveforms for eccentric binary black holes with nonprecessing spins, Phys. Rev. D **105**, 044035 (2022).

[116] H. Witek, L. Gualtieri, P. Pani, and T. P. Sotiriou, Black holes and binary mergers in scalar Gauss-Bonnet gravity: Scalar field dynamics, Phys. Rev. D **99**, 064035 (2019).

[117] M. Okounkova, L. C. Stein, M. A. Scheel, and D. A. Hemberger, Numerical binary black hole mergers in dynamical Chern-Simons gravity: Scalar field, Phys. Rev. D **96**, 044020 (2017).

[118] M. Okounkova, L. C. Stein, M. A. Scheel, and S. A. Teukolsky, Numerical binary black hole collisions in dynamical Chern-Simons gravity, Phys. Rev. D **100**, 104026 (2019).

[119] M. Okounkova, L. C. Stein, J. Moxon, M. A. Scheel, and S. A. Teukolsky, Numerical relativity simulation of GW150914 beyond general relativity, Phys. Rev. D **101**, 104016 (2020).

[120] M. Okounkova, Numerical relativity simulation of GW150914 in Einstein dilaton Gauss-Bonnet gravity, Phys. Rev. D **102**, 084046 (2020).

[121] M. Okounkova, M. Isi, K. Chatziioannou, and W. M. Farr, Gravitational wave inference on a numerical-relativity simulation of a black hole merger beyond general relativity, Phys. Rev. D **107**, 024046 (2023).

[122] W. E. East and J. L. Ripley, Evolution of Einstein-scalar-Gauss-Bonnet gravity using a modified harmonic formulation, Phys. Rev. D **103**, 044040 (2021).

[123] P. Figueras and T. França, Black hole binaries in cubic Horndeski theories, Phys. Rev. D **105**, 124004 (2022).

[124] L. Aresté Saló, K. Clough, and P. Figueras, Well-Posedness of the Four-Derivative Scalar-Tensor Theory of Gravity in Singularity Avoiding Coordinates, Phys. Rev. Lett. **129**, 261104 (2022).

[125] M. Corman, J. L. Ripley, and W. E. East, Nonlinear studies of binary black hole mergers in Einstein-scalar-Gauss-Bonnet gravity, Phys. Rev. D **107**, 024014 (2023).

[126] H. O. Silva, H. Witek, M. Elley, and N. Yunes, Dynamical Descalarization in Binary Black Hole Mergers, Phys. Rev. Lett. **127**, 031101 (2021).

[127] W. E. East and J. L. Ripley, Dynamics of Spontaneous Black Hole Scalarization and Mergers in Einstein-Scalar-Gauss-Bonnet Gravity, Phys. Rev. Lett. **127**, 101102 (2021).

[128] D. D. Doneva, A. Vañó Viñuales, and S. S. Yazadjiev, Dynamical descalarization with a jump during a black hole merger, Phys. Rev. D **106**, L061502 (2022).

[129] M. Elley, H. O. Silva, H. Witek, and N. Yunes, Spin-induced dynamical scalarization, descalarization, and stealthness in scalar-Gauss-Bonnet gravity during a black hole coalescence, Phys. Rev. D **106**, 044018 (2022).

[130] M. Punturo *et al.*, The Einstein Telescope: A third-generation gravitational wave observatory, Classical Quantum Gravity **27**, 194002 (2010).

[131] D. Reitze *et al.*, Cosmic Explorer: The U.S. contribution to gravitational-wave astronomy beyond LIGO, Bull. Am. Astron. Soc. **51**, 035 (2019).

[132] P. Amaro-Seoane *et al.* (LISA Collaboration), Laser interferometer space antenna, arXiv:1702.00786.

[133] C. Will and N. Yunes, *Is Einstein Still Right?: Black Holes, Gravitational Waves, and the Quest to Verify Einstein's Greatest Creation* (Oxford University Press, New York, 2020).

[134] gwosc.org.